

# On the weak-lensing masses of a new sample of galaxy groups

Elizabeth J. Gonzalez,<sup>1,2,3★</sup> Facundo Rodriguez<sup>1b</sup>,<sup>2,3</sup> Manuel Merchán,<sup>2,3</sup> Diego García Lambas,<sup>2,3</sup> Martín Makler,<sup>1,4</sup> Martín Chalela,<sup>2,3</sup> Maria E. S. Pereira,<sup>5</sup> Bruno Moraes<sup>6</sup> and HuanYuan Shan<sup>7,8</sup>

<sup>1</sup>Centro Brasileiro de Pesquisas Físicas, Rio de Janeiro, RJ 22290-180, Brazil

<sup>2</sup>Instituto de Astronomía Teórica y Experimental (IATE-CONICET), Laprida 854, X5000BGR Córdoba, Argentina

<sup>3</sup>Observatorio Astronómico de Córdoba, Universidad Nacional de Córdoba, Laprida 854, X5000BGR Córdoba, Argentina

<sup>4</sup>International Center for Advanced Studies & ICIFI (CONICET), ECyT-UNSAM, Campus Miguelete, 25 de Mayo y Francia, CP1650 Buenos Aires, Argentina

<sup>5</sup>Department of Physics, University of Michigan, Ann Arbor, MI 48109, USA

<sup>6</sup>Instituto de Física, Universidade Federal do Rio de Janeiro, RJ 21941-972, Rio de Janeiro, Brazil

<sup>7</sup>Shanghai Astronomical Observatory (SHAO), Nandan Road 80, Shanghai 200030, China

<sup>8</sup>University of Chinese Academy of Sciences, Beijing 100049, China

Accepted 2021 April 20. Received 2021 April 20; in original form 2021 January 12

## ABSTRACT

Galaxy group masses are important to relate these systems with the dark matter halo hosts. However, deriving accurate mass estimates is particularly challenging for low-mass galaxy groups. Moreover, calibration of observational mass-proxies using weak-lensing estimates have been mainly focused on massive clusters. We present here a study of halo masses for a sample of galaxy groups identified according to a spectroscopic catalogue, spanning a wide mass range. The main motivation of our analysis is to assess mass estimates provided by the galaxy group catalogue derived through an abundance matching luminosity technique. We derive total halo mass estimates according to a stacking weak-lensing analysis. Our study allows to test the accuracy of mass estimates based on this technique as a proxy for the halo masses of large group samples. Lensing profiles are computed combining the groups in different bins of abundance matching mass, richness, and redshift. Fitted lensing masses correlate with the masses obtained from abundance matching. However, when considering groups in the low- and intermediate-mass ranges, masses computed according to the characteristic group luminosity tend to predict higher values than the determined by the weak-lensing analysis. The agreement improves for the low-mass range if the groups selected have a central early-type galaxy. Presented results validate the use of mass estimates based on abundance matching techniques, which provide good proxies to the halo host mass in a wide mass range.

**Key words:** gravitational lensing; weak – galaxies; groups; general – dark matter..

## 1 INTRODUCTION

Galaxies tend to group together and form galaxy systems ranging from galaxy pairs to rich clusters. According to the current cosmological  $\Lambda$ CDM paradigm, these systems are expected to reside on highly overdense dark matter clumps, called haloes. In this context, galaxy systems are important to study galaxy evolution as well as constrain cosmological parameters within the standard paradigm (see e.g. Allen, Evrard & Mantz 2011; Kravtsov & Borgani 2012, for reviews). Therefore, reliable and complete group samples spanning a wide range of masses are important in order to study the evolution of these systems and use them as cosmological probes.

Commonly adopted galaxy group-finder algorithms are usually based on photometric properties such as photometric redshifts (e.g. van Breukelen & Clewley 2009; Milkeraitis et al. 2010; Soares-Santos et al. 2011; Wen, Han & Liu 2012; Durret et al. 2015; Radovich et al. 2017; Bellagamba et al. 2018) or on galaxy detection along the red-sequence (e.g. Gladders & Yee 2000; Gal et al. 2009; Murphy, Geach & Bower 2012; Oguri 2014; Rykoff et al.

2014; Licitra et al. 2016). These approaches have the advantage of running on large photometric data sets providing a large sample of mainly massive ( $\gtrsim 5 \times 10^{13} M_{\odot}$ ) galaxy groups. On the other hand, identification algorithms based on spectroscopic redshift information minimize biases introduced by projection effects on determining galaxy group memberships. Many algorithms based on spectroscopic surveys (Huchra & Geller 1982; Tucker et al. 2000; Merchán & Zandivarez 2002; Miller et al. 2005; Berlind et al. 2006; Yang et al. 2007; Tempel, Tago & Liivamägi 2012) have been successfully applied to provide group catalogues including systems with a low number of galaxy members i.e. low-mass systems ( $\gtrsim 5 \times 10^{12} M_{\odot}$ ).

Determining the group host halo mass is important in order to use galaxy systems as cosmological probes and to better characterize them. Given that the abundance and spatial distribution of galaxy systems is connected with the growth of structures within the cosmic expansion (see e.g. Kravtsov & Borgani 2012, for a review), comparing the observed distribution of galaxy systems in haloes mass bins to that expected in numerical simulations, can be used to constrain cosmological parameters. Moreover, it is expected that the baryonic processes taking place within the haloes are strongly related to their total mass (Le Brun et al. 2014). Hence, halo mass estimates

\* E-mail: ejgonzalez@unc.edu.ar

are also important to understand the effect of the environment on galaxy evolution.

In order to provide suitable group mass estimates, mass-proxies are usually considered including group richness, and X-ray and optical total luminosity. These relations are usually calibrated considering the masses estimated through the application of weak-lensing stacking techniques (e.g. Leauthaud et al. 2010; Viola et al. 2015; Simet et al. 2017; Pereira et al. 2018, 2020), since gravitational lensing provides a direct way to derive the average mass distribution for a sample of galaxy groups. These stacking techniques are based on the combination of groups within a range of a given observational property such as richness or total luminosity, in order to increase the signal-to-noise ratio of the lensing signal.

In general, studies linking weak-lensing halo masses to galaxy systems have been focused on massive or moderate-mass clusters, since low-mass galaxy groups are difficult to identify given their low number of bright members. Also, a higher dispersion between a mass-richness relation is expected for low-member galaxy groups and a correction to the apparent richness is needed in order to include faint galaxy members not targeted by the spectroscopic survey. Moreover, mass estimates are particularly challenging for these systems given that dynamical masses are not reliable because they are based on a small number of members, and X-ray luminosity studies are observationally difficult since they are significantly fainter in comparison to massive systems and, consequently samples are generally small (e.g. Sun et al. 2009; Eckmiller, Hudson & Reiprich 2011; Kettula et al. 2013; Finoguenov et al. 2015; Pearson et al. 2015). An alternative approach for mass estimates of low-mass systems comes from the assumption that there is a one-to-one relation between the characteristic group luminosity and the halo mass (Kravtsov et al. 2004; Tasitsiomi et al. 2004; Vale & Ostriker 2004; Conroy, Wechsler & Kravtsov 2006; Behroozi, Conroy & Wechsler 2010; Cristofari & Ostriker 2019). This approach for mass assignment is known as the abundance-matching technique and works by ordering the identified systems according to their characteristic luminosity and associating masses so that their abundance matches a theoretical mass function.

In this work, we analyse a sample of spectroscopic selected galaxy groups identified according to the algorithm presented by Rodriguez & Merchán (2020). The algorithm is based on a combination of percolation and halo-based methods. Groups were identified using the spectroscopic data of the Sloan Digital Sky Survey Data Release 12 (SDSS-DR12, Alam et al. 2015) and spans over a wide range of richness and masses, including a large fraction of low-richness galaxy systems. Taking into account the overabundance of low-mass systems, the inclusion of these systems in testing different mass proxies, is important for posterior cosmological analysis that comprise galaxy systems in a wide mass range.

For our analysis, we select a group sample from this catalogue and performed a weak-lensing analysis in order to estimate mean total halo masses. We consider the brightest galaxy member (BGM) as the halo centre and we model the possible miscentring effect on the lensing signal considering a fraction of miscentred groups. We also evaluate the relation between this fraction of groups and a wrong membership assignment using simulated data. Then, we compare derived masses with the estimates provided in the catalogue, computed according to both the abundance matching technique and the line-of-sight (LOS) velocity dispersion. We study the relation between these mass proxies and the lensing estimates and assess to which extent this relation is biased according to the group BGM morphology, redshift, and richness. Since the mass proxies provided in the catalogue rely on the membership assignment by the identification algorithm, the analysis allow us to test its performance

as well as to study the relation between the total halo masses and the mentioned proxies.

The paper is organized as follows: In Section 2, we describe the observational and simulated data used in this work, as well as the galaxy group catalogue. We detail in Section 3 the weak-lensing stacked analysis performed to derive the total halo masses. In Section 4, we present the results and study the relation between the mass proxies provided by the galaxy group catalogue and the lensing estimates. Finally, in Section 5, we summarize and discuss the results presented in this work. When necessary we adopt a standard cosmological model with  $H_0 = 70 \text{ km s}^{-1} \text{ Mpc}^{-1}$ ,  $\Omega_m = 0.3$ , and  $\Omega_\Lambda = 0.7$ .

## 2 DATA DESCRIPTION

### 2.1 Weak-lensing data

We perform the weak-lensing analysis by using a combination of the shear catalogues provided by four public weak-lensing surveys (Canada-France-Hawaii Telescope Lensing Survey [CFHTLenS], CS82, RCSLenS, and Kilo Degree Survey [KiDS]/KV450) based on similar quality observations, which allows the direct combination of these catalogues as done in previous works (Gonzalez et al. 2020; Schrabback et al. 2020; Xia et al. 2020). In this subsection, we first briefly describe the lensing surveys in which the shear catalogues are based and we also detail how we perform the galaxy background selection.

Although the combination of these surveys has been already tested in previous studies (see Appendix A in Gonzalez et al. 2020), we carried out the lensing analysis using the data of the individual surveys. Derived lensing masses for the individual surveys are all in agreement within  $2\sigma$  with the combined analysis, considering the errors for the individual mass estimates, and no significant bias are introduced. As complementary material in the Appendix A, we provide the resulting masses derived from the individual catalogues for the group sample. Masses are binned according to the abundance matching technique.

#### 2.1.1 Shear catalogues

The CFHTLenS weak-lensing catalogues<sup>1</sup> are based on observations provided by the CFHT Legacy Survey. This is a multiband survey ( $u^*g'r'iz'$ ) that spans  $154 \text{ deg}^2$  distributed in four separate patches W1, W2, W3, and W4 ( $63.8, 22.6, 44.2$ , and  $23.3 \text{ deg}^2$ , respectively). Considering a  $5\sigma$  point source detection, the limiting magnitude is  $i' \sim 25.5$ . The shear catalogue is based on the  $i$ -band measurements, with a weighted galaxy source density of  $\sim 15.1 \text{ arcmin}^{-2}$ . See Hildebrandt et al. (2012), Heymans et al. (2012), Miller et al. (2013), Erben et al. (2013) for further details regarding this shear catalogue.

The CS82 shear catalogue is based on the observations provided by the CFHT Stripe 82 survey, a joint Canada-France-Brazil project designed to complement the existing SDSS Stripe 82  $ugriz$  photometry with high-quality  $i$ -band imaging to be used for lensing measurements (Shan et al. 2014; Hand et al. 2015; Liu et al. 2015; Bundy et al. 2017; Leauthaud et al. 2017). This survey spans over a window of  $2 \times 80 \text{ deg}^2$ , with an effective area of  $129.2 \text{ deg}^2$ . It has a median point spread function (PSF) of  $0.6 \text{ arcsec}$  and a limiting magnitude  $i' \sim 24$  (Leauthaud et al. 2017). The source

<sup>1</sup>CFHTLenS: <http://www.cadc-ccda.hia-ihc.nrc-cnrc.gc.ca/en/community/CFHTLenS>.

galaxy catalogue has an effective weighted galaxy number density of  $\sim 12.3 \text{ arcmin}^{-2}$  and was constructed using the same weak-lensing pipeline developed by the CFHTLenS collaboration. Photometric redshifts are obtained using BPZ algorithm from matched SDSS co-add (Annis et al. 2014) and UKIDSS YJHK (Lawrence et al. 2007) photometry.

The RCSLenS catalogue<sup>2</sup> (Hilbrandt et al. 2016) is based on the Red-sequence Cluster Survey 2 (RCS-2, Gilbank et al. 2011). This is a multiband imaging survey in the *griz*-bands that reaches a depth of  $\sim 24.3$  in the *r*-band for a point source at  $7\sigma$  detection level and spans over  $\sim 785 \text{ deg}^2$  distributed in 14 patches, the largest being  $10 \times 10 \text{ deg}^2$  and the smallest  $6 \times 6 \text{ deg}^2$ . The source catalogue is based on *r*-band imaging and achieves an effective weighted galaxy number density of  $\sim 5.5 \text{ arcmin}^{-2}$ .

Finally, the KiDS-450 catalogue<sup>3</sup> (Hilbrandt et al. 2017) is based on the third data release of the KiDS (Kuijken et al. 2015), which is a multiband imaging survey (*ugri*) that spans over  $447 \text{ deg}^2$ . Shear catalogues are based on the *r*-band images with a mean PSF of  $0.68 \text{ arcsec}$  and a  $5\sigma$  limiting magnitude of  $25.0$ , resulting in an effective weighted galaxy number density of  $\sim 8.53 \text{ arcmin}^{-2}$ . Shape measurements are performed using an upgraded version of *lensfit* algorithm (Fenech Conti et al. 2017).

These data (except for KiDS-450) are based on imaging surveys carried-out using the MegaCam camera (Boulade et al. 2003) mounted on the *CFHT* therefore they have similar image quality. In spite that KiDS-450 shear catalogue is based on observations obtained with a different camera, both cameras share similar properties, such as a pixel scale of  $0.2 \text{ arcsec}$ . Also, the seeing conditions are similar for all the surveys ( $\sim 0.6 \text{ arcsec}$ ). Moreover, all the source galaxy catalogues were obtained using *lensfit* (Miller et al. 2007; Kitching et al. 2008) to compute the shape measurements and photometric redshifts are estimated using the BPZ algorithm (Benítez 2000; Coe et al. 2006). To combine the catalogues in the overlapping areas, we favour (disfavour) CFHTLenS (RCSLenS) data, since this catalogue is based in the deepest (shallowest) imaging, thus contain the highest (lowest) background galaxy density.

### 2.1.2 Galaxy background selection

For our analysis, we have only included galaxies considering the following *lensfit* parameters cuts:  $\text{MASK} \leq 1$ ,  $\text{FITCLASS} = 0$  and  $w > 0$ . Here MASK is a masking flag, FITCLASS is a flag parameter that is set to 0 when the source is classified as a galaxy, and  $w$  is a weight parameter that takes into account errors on the shape measurement and the intrinsic shape noise (see details in Miller et al. 2013). We carried out the lensing study by applying the additive calibration correction factors for the ellipticity components provided for each catalogue and a multiplicative shear calibration factor to the combined sample of galaxies as suggested by Miller et al. (2013).

For each group located at a redshift  $z$ , we select background galaxies, i.e. the galaxies that are located behind the group and thus affected by the lensing effect, taking into account  $\text{Z\_BEST} > z + 0.1$  and  $\text{ODDS\_BEST} > 0.5$ , where  $\text{Z\_BEST}$  is the photometric redshift estimated for each galaxy, and  $\text{ODDS\_BEST}$  is a parameter that expresses the quality of  $\text{Z\_BEST}$  and takes values from 0 to 1. We also restrict our galaxy background sample by considering the galaxies with  $\text{Z\_BEST} > 0.2$  and up to 1.2 for all the shear catalogues,

except for KiDS where a more restrictive cut is taken into account ( $\text{Z\_BEST} < 0.9$ ) according to the suggested by Hilbrandt et al. (2017). Background galaxies are assigned to each group using the public regular grid search algorithm *grispy*<sup>4</sup> (Chalela et al. 2019).

## 2.2 Galaxy groups

We use the publicly available galaxy group catalogue<sup>5</sup> obtained through the identification algorithm by Rodríguez & Merchán (2020), which combines friends-of-friends (FOF; Huchra & Geller 1982) and halo-based methods (Yang et al. 2005). This group finder aims to identify gravitationally bound galaxy systems with at least one bright galaxy, a galaxy with an absolute *r*-band,  $M_r$ ,<sup>6</sup> magnitude lower than  $-19.5$ . By so doing, we consider galaxy systems dominated by a central galaxy with fainter members that were not included in the spectroscopic catalogue. Briefly, the algorithm performs an iterative identification procedure that consists in two parts. First, all the galaxies with  $M_r < -19.5$  are linked using a FOF method based on spatial separation criteria following the prescriptions in Merchán & Zandivarez (2002, 2005). After this step, group candidates with at least one bright member are obtained.

Once the catalogue of potential groups is obtained, the membership assignment is optimized by applying a halo-based group finder following Yang et al. (2005, 2007). In this step, the algorithm computes a 3D density contrast in redshift space, taking into account a characteristic luminosity calculated according to the potential galaxy members. The characteristic luminosity,  $L_{\text{gr}}$ , associated to each group can be estimated from the luminosity of their galaxy members plus a correction that takes into account the incompleteness due to the limiting magnitude of the observational data (Moore, Frenk & White 1993).

Considering each group characteristic luminosity a halo mass is assigned,  $M_{\text{AM}}$ , performing an abundance matching technique on luminosity (e.g. Kravtsov et al. 2004; Tasitsiomi et al. 2004; Vale & Ostriker 2004; Conroy et al. 2006), which assumes a one-to-one relation between the mass and the luminosity. Taking this into account, masses are assigned after matching the rank orders of the halo masses and their characteristic luminosity for a given comoving volume, considering the Warren et al. (2006) halo mass function. A caveat is introduced at this stage, since the assumed halo mass function is cosmology dependent, which could introduce some biases when using the density distribution of groups binned in mass as cosmological probes. None the less, masses can be easily re-computed using another cosmology. It is important to highlight that, in spite this approach is based in the assumption of a one-to-one relation between the mass and the luminosity, masses are assigned after ranking the groups according to the computed  $L_{\text{gr}}$  and then matching the obtained distribution with the predicted taking into account the halo mass function.

After the mass assignment, the algorithm computes the 3D density contrast assuming that the distribution of galaxies in phase space follows that of the dark matter particles and adopting a Navarro-Frenk-White (NFW) profile to compute the projected density. The density contrast is estimated at the position of each potential member and only the galaxies that are located above a given threshold are considered as belonging to the system. Taking into account the

<sup>2</sup>RCSLenS: <https://www.cadc-ccda.hia-ihp.nrc-cnrc.gc.ca/en/community/rcslens>

<sup>3</sup>KiDS-450: <http://kids.strw.leidenuniv.nl/cosmicshear2018.php>.

<sup>4</sup><https://github.com/mchalela/GriSPy>

<sup>5</sup><http://iate.oac.uncor.edu/alcance-publico/catalogos/>

<sup>6</sup> $M_r$  is computed according to the SDSS apparent Petrosian magnitude and the galaxy spectroscopic redshift, considering the corresponding  $k$ -correction.



new membership assignment, a new characteristic luminosity is computed and the algorithm iterates until convergence in the number of members,  $N_{\text{GAL}}$ .

Galaxy groups are obtained by applying the algorithm to the spectroscopic galaxy catalogue provided by the SDSS-DR12. The catalogue includes 367 370 groups spanning from  $z \sim 0.02$  up to  $z = 0.3$ ; of which 302 392 with one member, 11 943 with four or more, and a 1386 with 10 or more members. Besides the mass estimate,  $M_{\text{AM}}$ , assigned during the identification procedure, the catalogue also provides for the groups with  $N_{\text{GAL}} \geq 4$ , the projected LOS velocity dispersion of the group,  $\sigma_v$  and a dynamical mass estimate,  $M_{\text{vir}}$ , computed following Merchán & Zandivarez (2002), according to  $\sigma_v$  and the position of each member.

We restrict the sample to the clusters that are included within the sky-coverage of the lensing catalogues. We also include in the analysis only the groups with  $\log M_{\text{AM}}/(h^{-1} M_{\odot}) > 12.5$ , to ensure we are considering group-scale haloes, and within a redshift range of  $0.05 < z < 0.2$ . The lower limit in the redshift is selected considering that the lensing signal decreases for groups at lower redshifts and the higher limit is selected taking into account that the sample of groups with  $N_{\text{GAL}} \geq 4$  extends up to  $z \sim 0.23$ . Applying these criteria, the total sample analysed comprises of 18 030 systems,  $\sim 63$  per cent of these are groups with  $N_{\text{GAL}} = 1$  and 1537 have more than four members ( $N_{\text{GAL}} \geq 4$ ). We have considered a subsample of these groups, hereafter *C*-sample, taking into account the morphology of the BGM according to the SDSS concentration index,  $C$ . This parameter is usually adopted to separate early- and late-type galaxies samples and is defined as  $C \equiv r_{90}/r_{50}$  (where  $r_{90}$  and  $r_{50}$  are the radii enclosing 90 per cent and 50 per cent of the  $r$ -band Petrosian flux, respectively). A sample of galaxies with  $C > 2.6$  is expected to include 75 per cent of early-type galaxies (Strateva et al. 2001). Therefore, we define the *C*-sample including groups with their BGM having  $C \geq 3.0$ , which roughly corresponds to the median value of the concentration distribution for the total sample of groups analysed. Furthermore, in order to explore the effects of variations of scaling relation between mass proxies for group samples with different mean redshift, we select two samples: a low redshift ( $z < 0.13$ ), and a high redshift ( $z \geq 0.13$ ) sample. In Fig. 1, we show the halo mass distribution,  $\log M_{\text{AM}}$ , for the total sample, the *C*-sample and other subsamples selected according to the number of members ( $N_{\text{GAL}} = 1$ ,  $2 \leq N_{\text{GAL}} \leq 3$ , and  $N_{\text{GAL}} \geq 4$ ). We also show the concentration index distribution for the group sample analysed. As it can be noticed, the concentration cut mainly discard low richness systems and so, bias the mass distribution to higher values.

### 2.3 Simulated data

As will be detailed in Section 3, for our lensing analysis, we assume that the halo centre can be well approximated by the BGM position. In order to test the effects of a wrong membership assignment introduced by the identification algorithm, we use a mock catalogue employing synthetic galaxies extracted from a semi-analytic model of galaxy formation applied on top of the Millennium Run Simulation I (Springel et al. 2005).

The Millennium Simulation is a cosmological  $N$ -body simulation that evolves more than 10 billion dark matter particles in a  $500 h^{-1}$  Mpc periodic box, using a comoving softening length of  $5 h^{-1}$  kpc. This simulation offers high spatial and time resolution within a large cosmological volume. This is a dark matter only simulation, but there are different models to populate haloes with galaxies. One of these is the semi-analytic galaxy formation model

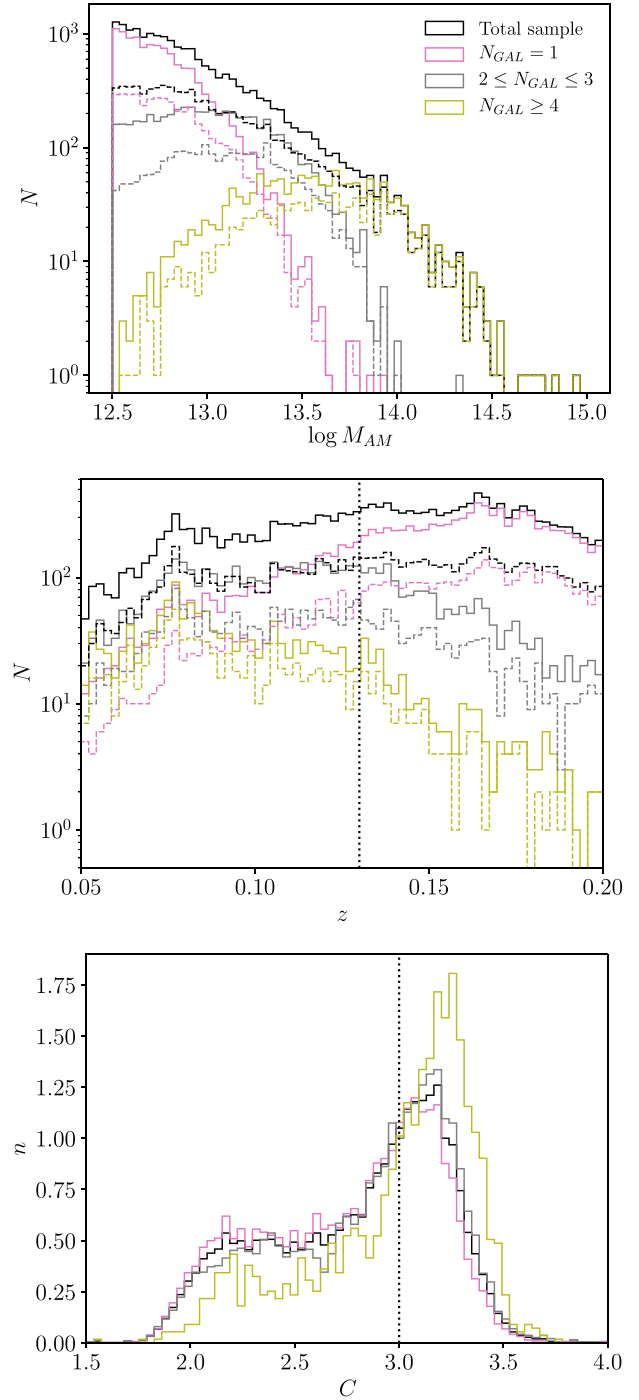


**Figure 1.** Upper panel and middle panel: Distribution of masses and redshift of the analysed samples of groups. Solid and dashed lines correspond to the mass distributions obtained for the total and *C*-sample, respectively. Dotted vertical in the middle panel indicates the  $z = 0.13$  limit used to select high- and low-redshift samples. Lower panel: Normalized distribution of the concentration index for the total sample of the groups analysed. The dotted vertical line at  $C = 3.0$  indicates the concentration value adopted to select the *C*-sample of groups. For all the panels, the coloured distributions correspond to different membership bins selected according to  $N_{\text{GAL}}$ .

developed by Guo et al. (2010), which we use to build our synthetic galaxy catalogue.

We construct our catalogue following the same procedure as in Rodriguez, Merchán & Sgró (2015) and Rodriguez & Merchán (2020). Since the Millenium simulation box is periodic, we place the observer at the coordinate origin and repeat the simulated volume until we reach the SDSS volume. The redshifts were obtained using the distances to the observer and taking into account the distortion produced by proper motions. Finally, to mimic SDSS, we impose the same upper apparent magnitude threshold of this catalogue and we use the mask to perform the same angular selection function of the survey.

We obtain the mock galaxy group catalogue by applying Rodriguez & Merchán (2020) identification algorithm with the same criteria as described in the previous subsection. In order to compute the shift of the centres due to the identification process, we match the halo to each group identified by our method, by looking for the maximum number of members in common. Then we compute the fraction of groups for which the brightest galaxy is located at the halo centre.

### 3 LENSING MASS ESTIMATES

#### 3.1 Adopted formalism

The weak gravitational lensing effect exerted by the mass distribution, associated to galaxy groups, produces a shape distortion of the background galaxies, resulting in an alignment of these galaxies in a tangential orientation with respect to the group centre. The introduced distortion by the lensing effect can be quantified by the shear parameter,  $\gamma = \gamma_1 + i\gamma_2$ , and can be estimated according to the measured ellipticity of background galaxies. The observed ellipticity results in a combination of the galaxy intrinsic shape and introduced by the lensing effect. Assuming that the galaxies are randomly orientated in the sky, the shear can be estimated by averaging the ellipticity of many sources,  $\langle e \rangle = \gamma$ . The noise introduced by the intrinsic shape of the sources can be reduced by using stacking techniques, which consists on combining several lenses that increase the density of sources. Stacking techniques effectively increase the signal-to-noise ratio of the shear measurements, allowing us to derive reliable average mass density distributions of the combined lenses (e.g. Leauthaud et al. 2017; Simet et al. 2017; Chalela et al. 2018; Pereira et al. 2020).

For a given projected mass density distribution, the azimuthally averaged tangential component,  $\gamma_t$ , of the shear can be related with the mass density contrast distribution following (Bartelmann 1995):

$$\gamma_t(r) \times \Sigma_{\text{crit}} = \bar{\Sigma}(< r) - \Sigma(r) \equiv \Delta\Sigma(r), \quad (1)$$

where we have defined the surface mass density contrast  $\Delta\Sigma$ . Here,  $\gamma_t(r)$  is the tangential component of the shear at a projected distance  $r$  from the centre of the mass distribution,  $\Sigma(r)$  is the projected mass surface density distribution, and  $\bar{\Sigma}(< r)$  is the average projected mass distribution within a disc at projected distance  $r$ .  $\Sigma_{\text{crit}}$  is the critical density defined as:

$$\Sigma_{\text{crit}} = \frac{c^2}{4\pi G} \frac{D_{OS}}{D_{OL} D_{LS}}, \quad (2)$$

where  $D_{OL}$ ,  $D_{OS}$ , and  $D_{LS}$  are the angular diameter distances from the observer to the lens, from the observer to the source, and from the lens to the source, respectively.

To model the surface density distribution of the halo,  $\Sigma$ , we use the usual NFW profile (Navarro, Frenk & White 1997). This model depends on two parameters: the radius that encloses the mean density

equal to 200 times the critical density of the Universe,  $R_{200}$ , and a dimensionless concentration parameter,  $c_{200}$ . The density profile is defined as:

$$\rho(r) = \frac{\rho_{\text{crit}} \delta_c}{(r/r_s)(1 + r/r_s)^2}, \quad (3)$$

where  $r_s$  is the scale radius,  $r_s = R_{200}/c_{200}$ ,  $\rho_{\text{crit}}$  is the critical density of the Universe at the mean redshift of the sample of stacked galaxy groups,  $\langle z \rangle$ , and  $\delta_c$  is the characteristic overdensity of the halo:

$$\delta_c = \frac{200}{3} \frac{c_{200}^3}{\ln(1 + c_{200}) - c_{200}/(1 + c_{200})}. \quad (4)$$

We compute  $\langle z \rangle$  by averaging the group sample redshifts, weighted according to the number of background galaxies considered for each group. The mass within  $R_{200}$  can be obtained as  $M_{200} = 200 \rho_{\text{crit}} (4/3) \pi R_{200}^3$ . The lensing formula adopted to model this profile is described by Wright & Brainerd (2000). In the fitting procedure, we use a fixed mass-concentration relation  $c_{200}(M_{200}, z)$ , derived from simulations by Duffy et al. (2008):

$$c_{200} = 5.71 (M_{200}/2 \times 10^{12} h^{-1})^{-0.084} (1 + \langle z \rangle)^{-0.47}. \quad (5)$$

This approach is applied since the concentration parameter mainly affects the slope in the inner regions of the profile and therefore is poorly constrained. Nevertheless, as shown in previous studies, the particular choice of this relation does not have a significant impact on the final mass values, which have uncertainties dominated by the noise of the shear profile (Rodriguez et al. 2020).

To compute the profiles, we adopt as the group centre, the position of the BGM. The offset distribution between these galaxy-based centres and the true halo centre can be described by considering two group sample populations: well-centred and miscentred groups (Yang et al. 2006; Johnston et al. 2007; Ford et al. 2014; Yan et al. 2020). This miscentring affects the observed shear profile by flattening the lensing signal at the inner regions. We consider the miscentring effect in our analysis by modelling the contrast density distribution taking into account two terms:

$$\Delta\Sigma = p_{\text{cc}} \Delta\Sigma_{\text{cen}} + (1 - p_{\text{cc}}) \Delta\Sigma_{\text{mis}}, \quad (6)$$

where  $\Delta\Sigma_{\text{cen}}$  and  $\Delta\Sigma_{\text{mis}}$  correspond to the contrast density distribution for a perfectly centred, and a miscentred dark matter distribution, respectively, and  $p_{\text{cc}}$  is the fraction of well-centred clusters.  $\Delta\Sigma_{\text{cen}}$  is obtained as:

$$\Delta\Sigma_{\text{cen}}(r) = \bar{\Sigma}(< r) - \Sigma(r). \quad (7)$$

The miscentring term,  $\Delta\Sigma_{\text{mis}}$ , is modelled following Yang et al. (2006), Johnston et al. (2007), and Ford et al. (2014). An axis-symmetric surface mass density distribution whose centre is offset by  $r_s$ , with respect to the adopted centre in the lens plane, results in a projected average density profile given by:

$$\Sigma(r|r_s) = \frac{1}{2\pi} \int_0^{2\pi} \Sigma \left( \sqrt{r^2 + r_s^2 + 2rr_s \cos \theta} \right) d\theta. \quad (8)$$

The fraction of miscentred groups is expected to be shifted following a Gaussian distribution, therefore the projected offsets can be modelled according to a Rayleigh distribution:

$$P(r_s) = \frac{r_s}{\sigma_{\text{off}}^2} \exp \left( -\frac{1}{2} \frac{r_s^2}{\sigma_{\text{off}}^2} \right). \quad (9)$$

Alternatively, we have also considered a Gamma function with shape parameter  $k = 2$  to model the offset distribution:

$$P(r_s) = \frac{r_s}{\sigma_{\text{off}}^2} \exp \left( -\frac{r_s}{\sigma_{\text{off}}} \right). \quad (10)$$

We consider this model based on the recent work of Yan et al. (2020) where they study the miscentring effect by considering different proxies using hydrodynamic simulations.

Taking this into account, the miscentred density can be computed as follows:

$$\Sigma_{mis}(r) = \int_0^\infty P(r_s) \Sigma(r|r_s) dr_s, \quad (11)$$

such that the miscentring term for the density contrast profile is:

$$\Delta \Sigma_{mis}(r) = \tilde{\Sigma}_{miss}(< r) - \Sigma_{mis}(r). \quad (12)$$

### 3.2 Computed estimator and fitting procedure

We compute the density contrast distribution profiles by averaging the tangential ellipticity component of the background galaxies of each group considered in the stacking, as:

$$\Delta \tilde{\Sigma}(r) = \frac{\sum_{j=1}^{N_L} \sum_{i=1}^{N_{S,j}} \omega_{LS,ij} \Sigma_{crit,ij} e_{t,ij}}{\sum_{j=1}^{N_L} \sum_{i=1}^{N_{S,j}} \omega_{LS,ij}}, \quad (13)$$

where  $\omega_{LS,ij}$  is the inverse variance weight computed according to the weight,  $\omega_{ij}$ , given by the *lensfit* algorithm for each background galaxy,  $\omega_{LS,ij} = \omega_{ij} / \Sigma_{crit,ij}^2$ .  $N_L$  is the number of galaxy groups considered for the stacking and  $N_{S,j}$  the number of background galaxies located at a distance  $r \pm \delta r$  from the  $j$ th group.  $\Sigma_{crit,ij}$  is the critical density for the  $i$ -th background galaxy of the  $j$ -th group. The inner regions of the profile could be affected by a stellar mass contribution of the central galaxies. Moreover, these regions are more affected by the background selection and an increased scatter to low sky area in the inner regions. Taking these facts into account, we obtain the profiles by binning the background galaxies in 15 non-overlapping log-spaced  $r$  bins, from  $300 h^{-1}$  kpc up to  $5 h^{-1}$  Mpc.

Errors in the photometric redshifts can led to the inclusion of foreground or galaxy members in the background galaxy sample. These galaxies are unlensed and result in an underestimated density contrast, which is called as the dilution effect. In order to take this effect into account, the  $\Delta \tilde{\Sigma}$  measurement can be boosted to recover the corrected signal by using the so-called *boost-factor* (Kneib et al. 2003; Sheldon et al. 2004; Applegate et al. 2014; Hoekstra et al. 2015; Leauthaud et al. 2017; Melchior et al. 2017; Simet et al. 2017; McClintock et al. 2019; Varga et al. 2019; Pereira et al. 2020):  $1/(1 - f_{cl})$ , where  $f_{cl}$  is the cluster contamination fraction and it is expected to be higher in the inner radial bins where the contamination by cluster members is more significant. We compute  $f_{cl}$  by using a similar approach as the presented in Hoekstra (2007). Since a non-contaminated background galaxy sample will present a constant density for all the considered radial bins, by computing the excess in the density at each considered radial bin, we obtain an estimated value of  $f_{cl}$ . This excess is computed taking into account the background galaxy density obtained for the last radial bin at  $5 h^{-1}$  Mpc, where the contamination of unlensed galaxies is expected to be negligible. By doing so, we obtain the  $f_{cl}(r)$  fraction which is included in the analysis. The inclusion of the *boost-factor* in the analysis result in higher mass estimates by a  $\sim 10$  per cent ( $\sim 25$  per cent) for the lowest (highest) mass bin sample of groups.

In order to estimate the group halo masses, we fit the computed profiles with the adopted model (equation 6) considering the two free parameters,  $p_{cc}$  and  $M_{WL}$  (where  $M_{WL}$  is the  $M_{200c}$  mass). We fix the width of the offset distributions,  $\sigma_{off}$ , in terms of the radius,  $R_{AM}$ , which is the  $R_{200}$  radius estimated from the abundance matching mass  $M_{AM}$ , which are expected to be related (Simet et al. 2017). Thus, we set  $\sigma_{off} = 0.4 \times R_{AM}$  in equation (9) according to the

results presented in Simet et al. (2017). On the other hand, the offset dispersion in equation (10) is given by  $\sigma_{off} = 0.3 \times R_{AM}$  from Yan et al. (2020). This approach is similar to the one applied in the fitting procedure of previous stacking analysis (Simet et al. 2017; Pereira et al. 2018; McClintock et al. 2019; Pereira et al. 2020) in which  $\sigma_{off}$  is fitted considering a radius computed according to the richness estimator. Although this parameter is fixed taking into account the radius derived according to the  $M_{AM}$  mass estimate, we also try fitting this parameter together with the mass estimate,  $\sigma_{off} = 0.4 \times R_{WL}$  and  $\sigma_{off} = 0.3 \times R_{WL}$ . The resultant fitted parameters,  $p_{cc}$  and  $M_{WL}$ , were in agreement with the previous estimates but less constrained. Therefore our final masses do not strongly depend on  $\sigma_{off}$ . We highlight that the fitted miscentring term can also be affected by the adopted concentration,  $c_{200}$ , since this parameter impacts in the slope profile. We also neglect the contribution of the two-halo term, introduced by the contribution of neighbouring haloes, by fitting the profiles up to a limiting projected radius of  $R_{OUT}$ . This radius is estimated according to the relation presented by Simet et al. (2017) to compute the upper limit radius taking into account  $M_{AM}$ . For the highest mass bins considered in the analysis, where the lack of modelling of the two-halo term can biases the lensing mass estimates, we adopt a more restrictive limiting radius of  $2.5 h^{-1}$  Mpc. Thus, all the profiles are fitted up to  $\min(R_{OUT}, 2.5 h^{-1} \text{ Mpc})$ .

We constrain our free parameters,  $p_{cc}$  and  $M_{WL}$ , by using the Markov chain Monte Carlo method, implemented through EMCEE PYTHON package (Foreman-Mackey et al. 2013) to optimize the log-likelihood function for the density contrast profile,  $\ln \mathcal{L}(\Delta \Sigma | r, M_{WL}, p_{cc})$ . We fit the data by using 10 walkers for each parameter and 500 steps, considering flat priors for the mass and the fraction of well-centred groups,  $11.5 < \log(M_{WL}/(h^{-1} M_\odot)) < 16$  and  $0.2 < p_{cc} < 1.0$ . We adopt as the best-fitting parameters the median value of the posterior distributions and the correspondent errors are based on the differences between the median and the 16th and 84th percentiles, without considering the first 100 steps of each chain. We show in Figs 2 and 3 the computed profiles together with the fitted models, for the subsamples selected in  $\log M_{AM}$  bins from the total sample and the C-sample, respectively.

## 4 RESULTS

In this section, we first discuss the adopted miscentring modelling and compare the lensing results to numerical simulations. Then, we compare the derived lensing masses to the mass estimates provided by the group catalogue,  $M_{AM}$ , computed according to the abundance matching assignment. We also study biases in group masses for the different subsamples selected considering the group richness and redshift. Finally, for the groups with  $N_{GAL} \geq 4$ , we compare derived lensing mass estimates to the projected LOS velocity dispersion,  $\sigma_v$ .

In order to study the relation between the abundance matching masses and the lensing estimates, we split the total sample and the C-sample of groups in seven  $\log M_{AM}$  bins from  $10^{12.5}$  up to  $10^{15} h^{-1} M_\odot$ . We also obtain the lensing masses considering the richness subsamples defined in Section 2.2 and high- and low-redshift subsamples. In Tables 1 and 2, we describe the selection criteria together with the best-fitting parameters for the samples selected according to the richness and redshift, respectively. In Appendix B, we show the 2D posterior probability distributions for the total sample. We also show in Appendix C the characteristic luminosity distributions, their medians and 15th and 85th percentiles for each considered bin. Derived lensing masses for the subsamples range from  $3 \times 10^{12}$  to  $5 \times 10^{14} h^{-1} M_\odot$ . Therefore, our analysis spans

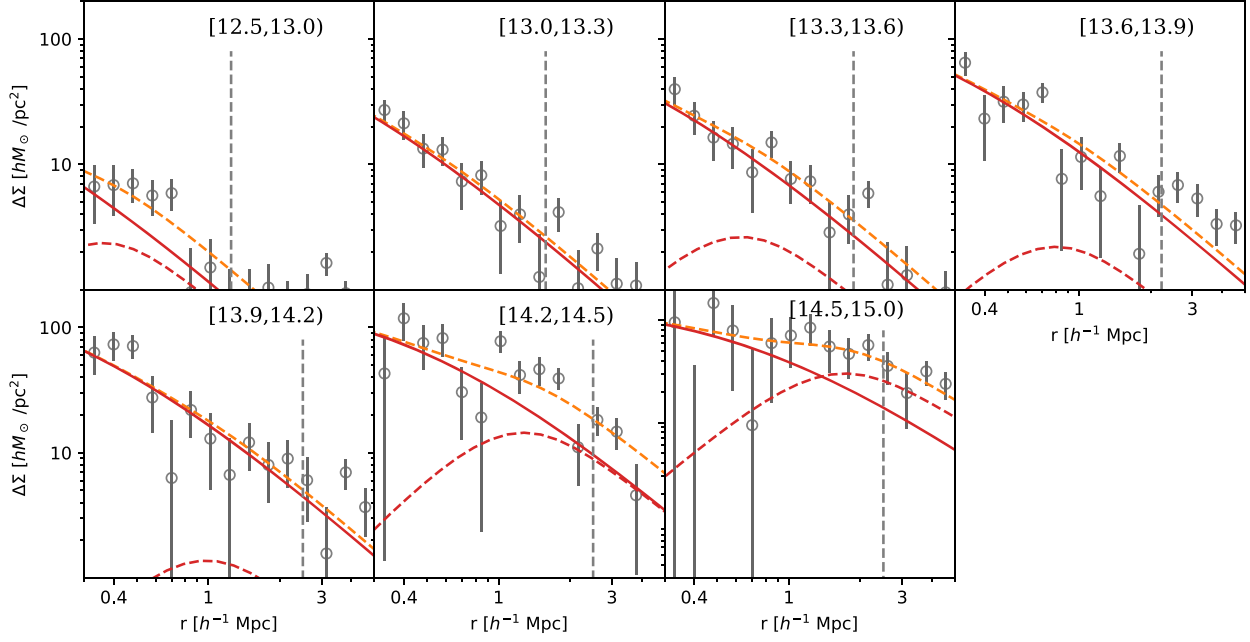


**Figure 2.** Contrast density profiles for the subsamples selected from the total sample in the whole richness and redshift range ( $N_{\text{GAL}} \geq 1$  and  $0.05 \leq z < 0.2$ ). Labels indicate the  $\log M_{\text{AM}}$  bin. Dashed orange lines corresponds to the total fitted profile (equation 6) and solid and dashed red lines corresponds to the centred,  $\Delta \Sigma_{\text{cen}}$  (equation 7), and the miscentring terms,  $\Delta \Sigma_{\text{mis}}$  (equation 12), respectively. Offset distributions are computed according to equation (9). Vertical dashed lines correspond to the upper limit in the projected radius adopted in the fitting procedure.

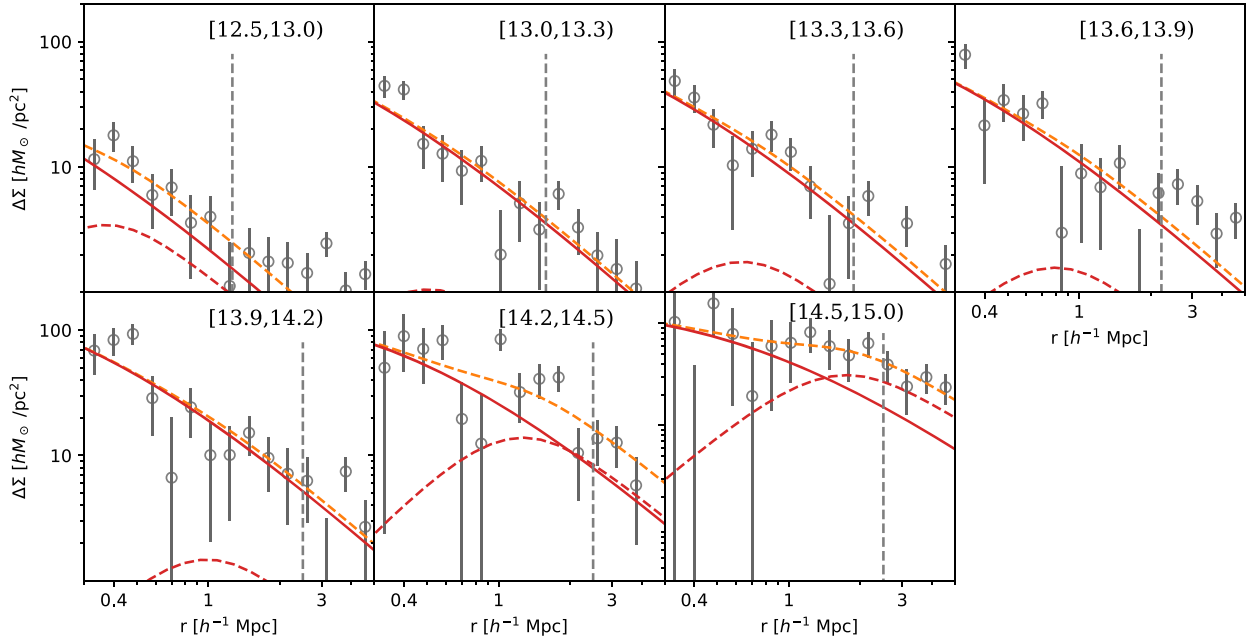


**Figure 3.** Idem as in Fig. 2 but for subsamples selected from the C-sample in the whole richness and redshift range ( $N_{\text{GAL}} \geq 1$  and  $0.05 \leq z < 0.2$ ).

over a wide range of halo masses. We further discuss the results obtained in the next subsections.

#### 4.1 Miscentring study

Taking into account the two different expressions (equations 9 and 10) to model the offset distribution of the miscentred groups, we

fit two sets of free parameters,  $p_{\text{cc}}$  and  $M_{\text{WL}}$ , for each model. We find no significant differences between the reduced chi-square values obtained from both offset modelling, obtaining a mean of the reduced chi-square ratios of 0.99, and a standard deviation of 0.02. Moreover, the fitting parameters are in excellent mutual agreement, since the mean ratio of  $M_{\text{WL}} (p_{\text{cc}})$  is 1.05 (1.04) with a standard deviation of 0.05 (0.08). Therefore, both modellings provide



**Table 1.** Fitted parameters for the analysed galaxy groups in the whole redshift range ( $0.05 \leq z < 0.2$ ).

Richness Selection	$\log M_{AM}$ [ $\log (h^{-1} M_{\odot})$ ]	$N_L$	Total sample $M_{WL}$ [ $10^{13} h^{-1} M_{\odot}$ ]	$p_{cc}$	$N_L$	C-sample $M_{WL}$ [ $10^{13} h^{-1} M_{\odot}$ ]	$p_{cc}$
$N_{GAL} \geq 1$	[12.5, 13.0]	12647	$0.31^{+0.05}_{-0.07}$	$0.57^{+0.26}_{-0.25}$	4421	$0.60^{+0.10}_{-0.14}$	$0.62^{+0.26}_{-0.28}$
	[13.0, 13.3]	3093	$0.95^{+0.13}_{-0.15}$	$0.90^{+0.08}_{-0.14}$	1551	$1.48^{+0.19}_{-0.22}$	$0.91^{+0.07}_{-0.15}$
	[13.3, 13.6]	1406	$1.81^{+0.27}_{-0.28}$	$0.75^{+0.15}_{-0.18}$	832	$2.14^{+0.30}_{-0.39}$	$0.85^{+0.11}_{-0.17}$
	[13.6, 13.9]	571	$3.4^{+0.5}_{-0.5}$	$0.83^{+0.12}_{-0.15}$	380	$2.80^{+0.51}_{-0.63}$	$0.86^{+0.10}_{-0.15}$
	[13.9, 14.2]	236	$4.5^{+0.9}_{-0.8}$	$0.88^{+0.09}_{-0.16}$	178	$5.3^{+1.0}_{-1.0}$	$0.89^{+0.08}_{-0.16}$
	[14.2, 14.5]	68	$21^{+4}_{-4}$	$0.50^{+0.17}_{-0.14}$	50	$18^{+5}_{-4}$	$0.47^{+0.16}_{-0.15}$
	[14.5, 15.0]	9	$61^{+19}_{-25}$	$0.32^{+0.14}_{-0.08}$	7	$66^{+19}_{-23}$	$0.32^{+0.17}_{-0.09}$
$N_{GAL} = 1$	[12.5, 12.9]	8815	$0.34^{+0.07}_{-0.09}$	$0.52^{+0.25}_{-0.28}$	2894	$0.56^{+0.14}_{-0.15}$	$0.65^{+0.25}_{-0.28}$
	[12.9, 13.1]	1703	$0.70^{+0.17}_{-0.20}$	$0.75^{+0.16}_{-0.28}$	810	$1.35^{+0.25}_{-0.39}$	$0.79^{+0.16}_{-0.28}$
	[13.1, 13.5]	748	$1.70^{+0.37}_{-0.40}$	$0.82^{+0.12}_{-0.20}$	442	$2.17^{+0.45}_{-0.51}$	$0.84^{+0.12}_{-0.20}$
$2 \leq N_{GAL} \leq 3$	[12.5, 13.5]	4843	$0.56^{+0.12}_{-0.11}$	$0.57^{+0.18}_{-0.25}$	2069	$1.12^{+0.20}_{-0.22}$	$0.73^{+0.18}_{-0.25}$
	[13.5, 14.5]	357	$3.8^{+0.7}_{-0.6}$	$0.79^{+0.07}_{-0.18}$	237	$3.7^{+0.7}_{-0.7}$	$0.90^{+0.07}_{-0.18}$
$N_{GAL} \geq 4$	[12.5, 13.8]	1113	$1.29^{+0.28}_{-0.31}$	$0.68^{+0.14}_{-0.22}$	639	$1.31^{+0.33}_{-0.36}$	$0.81^{+0.14}_{-0.22}$
	[13.8, 14.2]	348	$3.9^{+0.7}_{-0.6}$	$0.90^{+0.07}_{-0.14}$	255	$4.8^{+0.7}_{-0.8}$	$0.90^{+0.07}_{-0.14}$
	[14.2, 15.5]	75	$28^{+4}_{-5}$	$0.42^{+0.17}_{-0.10}$	56	$26^{+4}_{-5}$	$0.36^{+0.17}_{-0.10}$

Columns: (1) Richness range of the selected subsamples; (2) Selection criteria according to the abundance matching mass,  $M_{AM}$ ; (3), (4), and (5) number of groups considered in the stacked sample and fitted parameters,  $M_{WL}$  and  $p_{cc}$ , for the total sample of groups. (6), (7), and (8) same for the groups included in the C-sample.**Table 2.** Fitted parameters for the analysed galaxy groups in the whole richness range ( $N_{GAL} \geq 1$ ).

Redshift Selection	$\log M_{AM}$ [ $\log (h^{-1} M_{\odot})$ ]	$N_L$	Total sample $M_{WL}$ [ $10^{13} h^{-1} M_{\odot}$ ]	$p_{cc}$	$N_L$	C-sample $M_{WL}$ [ $10^{13} h^{-1} M_{\odot}$ ]	$p_{cc}$
$z < 0.13$	[12.5, 13.0]	5186	$0.25^{+0.08}_{-0.12}$	$0.56^{+0.28}_{-0.25}$	1963	$0.41^{+0.14}_{-0.22}$	$0.57^{+0.30}_{-0.26}$
	[13.0, 13.3]	1317	$0.70^{+0.18}_{-0.22}$	$0.69^{+0.22}_{-0.27}$	679	$1.28^{+0.28}_{-0.35}$	$0.85^{+0.11}_{-0.20}$
	[13.3, 13.6]	639	$1.18^{+0.30}_{-0.39}$	$0.74^{+0.18}_{-0.27}$	389	$1.34^{+0.38}_{-0.50}$	$0.72^{+0.20}_{-0.25}$
	[13.6, 13.9]	288	$1.58^{+0.54}_{-0.68}$	$0.65^{+0.23}_{-0.28}$	206	$1.54^{+0.61}_{-0.75}$	$0.63^{+0.23}_{-0.27}$
	[13.9, 14.2]	144	$4.1^{+0.9}_{-1.0}$	$0.86^{+0.10}_{-0.17}$	112	$4.5^{+1.1}_{-1.2}$	$0.89^{+0.08}_{-0.15}$
	[14.2, 14.5]	43	$22^{+5}_{-6}$	$0.42^{+0.19}_{-0.13}$	32	$20^{+5}_{-6}$	$0.42^{+0.23}_{-0.15}$
	[14.5, 15.0]	6	$14^{+15}_{-54}$	$0.57^{+0.28}_{-0.27}$	4	$10.0^{+15.7}_{-45.9}$	$0.60^{+0.26}_{-0.26}$
$z \geq 0.13$	[12.5, 13.0]	7461	$0.31^{+0.07}_{-0.08}$	$0.69^{+0.21}_{-0.30}$	2458	$0.64^{+0.12}_{-0.15}$	$0.72^{+0.21}_{-0.30}$
	[13.0, 13.3]	1776	$1.26^{+0.18}_{-0.21}$	$0.86^{+0.11}_{-0.20}$	872	$1.80^{+0.29}_{-0.41}$	$0.84^{+0.12}_{-0.22}$
	[13.3, 13.6]	767	$2.13^{+0.43}_{-0.43}$	$0.70^{+0.20}_{-0.24}$	443	$2.83^{+0.51}_{-0.52}$	$0.79^{+0.15}_{-0.19}$
	[13.6, 13.9]	283	$5.3^{+0.7}_{-0.8}$	$0.90^{+0.08}_{-0.14}$	174	$4.8^{+0.9}_{-0.8}$	$0.88^{+0.09}_{-0.15}$
	[13.9, 14.2]	92	$5.6^{+1.6}_{-1.8}$	$0.72^{+0.19}_{-0.24}$	66	$7.2^{+2.0}_{-2.2}$	$0.74^{+0.18}_{-0.23}$
	[14.2, 14.5]	25	$21^{+6}_{-6}$	$0.67^{+0.21}_{-0.20}$	18	$20^{+6}_{-7}$	$0.67^{+0.22}_{-0.25}$
	[14.5, 15.0]	3	$68^{+23}_{-30}$	$0.37^{+0.20}_{-0.11}$	3	$66^{+22}_{-29}$	$0.39^{+0.25}_{-0.13}$

Columns: (1) Redshift range of the selected subsamples; (2) Selection criteria according to the abundance matching mass,  $M_{AM}$ ; (3), (4), and (5) number of groups considered in the stacked sample and fitted parameters,  $M_{WL}$  and  $p_{cc}$ , for the total sample of groups. (6), (7), and (8) same for the groups included in the C-sample.

consistent profiles within the fitting parameter uncertainties. For the rest of our analysis, we consider only the parameters derived taking into account equation (9).

In order to test if the results are consistent with the expected miscentring due to a wrong membership assignation by the identification algorithm, we use the mock sample of groups described in Section 2.3. We compute the projected distance distribution between the central galaxy of the halo and the brightest member assigned

to the group hosted by the halo. Then, we compute the fraction of well-centred groups in bins of  $\log M_{AM}$ , i.e. the fraction of groups of which the BGM is the central galaxy of the dark matter host halo. We also fit equations (9 and 10) to the distributions of projected distances, to estimate the dispersion,  $\sigma_{off}$ . Estimated dispersion values of the Rayleigh distribution are systematically higher than the dispersion fitted using a Gamma distribution by a factor  $\sim 1.4$ , with a mean  $\sigma_{off}$  of 0.4 and 0.3, respectively. This



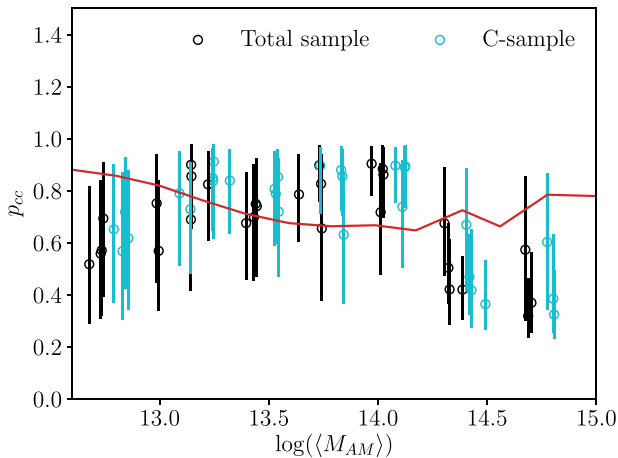


**Figure 4.** Fraction of well-centred galaxy groups,  $p_{cc}$ , fitted according to the density contrast profiles for the considered samples detailed in Tables 1 and 2 as a function of the mean  $M_{AM}$ . The red solid line is the fraction obtained from the simulated data, which considers the expected miscentred introduced by a wrong membership assignment. For the C-samples, values are shifted in the x-axis by 0.1 for a better visualization of the figure.

supports the adopted fixed values for  $\sigma_{off}$  stated in the previous section.

In Fig. 4, we show the  $p_{cc}$  values obtained from the lensing analysis together with that derived from the mock sample as a function of the mean  $M_{AM}$  for each bin. No significant differences are obtained when considering the C-sample. For the observed group sample, as well as for the groups identified in the simulation, the fraction of well-centred groups tend to decrease with the mean mass. Although there is a general agreement between  $p_{cc}$  estimates derived from the simulated sample and the lensing estimates, these later estimates tend to be systematically biased to lower values for massive systems ( $>10^{14} h^{-1} M_{\odot}$ ) which are expected to include a larger fraction of merging systems. It is important to highlight that the analyses based on the simulated data only takes into account the miscentred introduced by errors in the membership assignation, thus, it does not considers possible offsets between the dark matter halo and the BGM centres due to gas/galaxy dynamics. On the other hand, lensing  $p_{cc}$  values result from a combination of both effects.

#### 4.2 Relating lensing masses to the abundance matching prediction

In Figs 5 and 6, we show the relation between the average  $M_{AM}$  and the lensing masses,  $M_{WL}$ , for the subsamples detailed in Tables 1 and 2. In order to interpret the results, we define three mass regimes, the low-mass that includes groups with  $\langle M_{AM} \rangle < 10^{13.3} h^{-1} M_{\odot}$ , the intermediate-mass that considers groups with  $10^{13.3} h^{-1} M_{\odot} < \langle M_{AM} \rangle < 10^{14.2} h^{-1} M_{\odot}$  and the high-mass regime with groups that have  $\langle M_{AM} \rangle > 10^{14.2} h^{-1} M_{\odot}$ .

There is an excellent correlation between both mass estimates for all the subsamples considered. Nevertheless, for the subsamples selected in the whole redshift and richness range from the total sample of groups (empty black dots in both figures), lensing masses are systematically underestimated for low- and intermediate-mass groups by a factor  $\sim 0.6$ . When considering the groups from the C-sample, we obtain a better agreement between both mass estimates for the low-mass subsamples. In Fig. 7, we compare lensing mass estimates considering the total and C-sample. For the C-sample, we expect higher lensing mass estimates since this selection proxy

could improve the group selection, by considering systems with an elliptical brightest galaxy, since this morphological galaxy type is more related with denser environments. As it can be noticed, lensing estimates are all in excellent agreement for all the groups with  $\langle M_{AM} \rangle \geq 10^{13.3} h^{-1} M_{\odot}$ . On the other hand, for low-mass groups, lensing masses are about a factor two higher when the BGM is an early-type galaxy. This is expected since the applied cut in the concentration index affects mainly this mass range (see Fig. 1).

When considering a group richness binning to infer halo mass lensing estimates, the subsamples that include groups with low-richness ( $N_{GAL} \leq 3$ ) follow the trend found in the low-mass regime. Contrarily, at the intermediate-mass range, which includes a richer range,  $N_{GAL} \geq 4$ , group masses show lower lensing estimates compared to  $\langle M_{AM} \rangle$ . For this range of masses and richness, we expect a higher contamination by interlopers, since the purity of the group identification algorithm is lower at these ranges (see fig. 1 from Rodríguez & Merchán 2020). This could bias the abundance matching masses to higher values since a higher total luminosity is assigned.

Finally, when the subsamples are selected according to the group redshift, we obtain systematically higher lensing masses for the high redshift sample. Although both masses are in agreement within  $1.5\sigma$  for the low- and high-mass regimes, for intermediate-mass groups at higher redshift, we obtain up to three times higher lensing masses than for the groups located at lower redshift. These discrepancies can be related with the observed differences when selecting the subsamples according to the richness, since intermediate-mass groups with  $N_{GAL} \geq 4$  are mainly located at lower redshifts (see Fig. 1). In this mass range, 75 per cent (21 per cent) of the groups located at  $z < 0.13$  ( $z \geq 0.13$ ) have  $N_{GAL} \geq 4$ .

#### 4.3 Relating lensing masses with the LOS velocity dispersion

Usually adopted mass estimates for low-richness galaxy systems are based on the dynamics of galaxies. These estimates are computed through spectroscopic redshifts and angular positions of galaxy members. We have compared our derived lensing halo masses to the median  $\sigma_V$  provided in the catalogue for groups with  $N_{GAL} \geq 4$ . (Fig. 8). A good correlation is observed between these parameters. According to numerical simulations, a virial scaling relation of the form ( $M \propto \sigma^3$ ; Evrard et al. 2008) is expected between these parameters. Nevertheless, a lower slope was found from previous weak-lensing analysis ( $M \propto \sigma^2$ ; Han et al. 2015; Viola et al. 2015). According to Viola et al. (2015), the observed shallower mass-velocity relation is mostly related to selection effects of the group sample. On the other hand, our results (Fig. 8) are more compatible with a steeper relation.

It is important to highlight that  $\sigma_V$  depend crucially on membership assignment. The inclusion of interlopers might bias the velocity dispersion to higher values. Moreover, virial mass estimates assume that the group/clusters are in dynamical equilibrium. According to the results discussed in the previous subsection, higher mass haloes include a larger fraction of miscentred groups. Thus, the highest mass bin sample may contain a larger fraction of merging systems. Another drawback about the dynamical estimates relies on the simplicity of the model assumed to compute the masses, since the relation between the projected velocity dispersion and the mass is held only up to the virial radius (Alpaslan et al. 2012). Nevertheless and in spite of these possible bias, the observed good correlation between both parameters suggests that  $\sigma_V$  provides a suitable proxy for the mean halo mass.

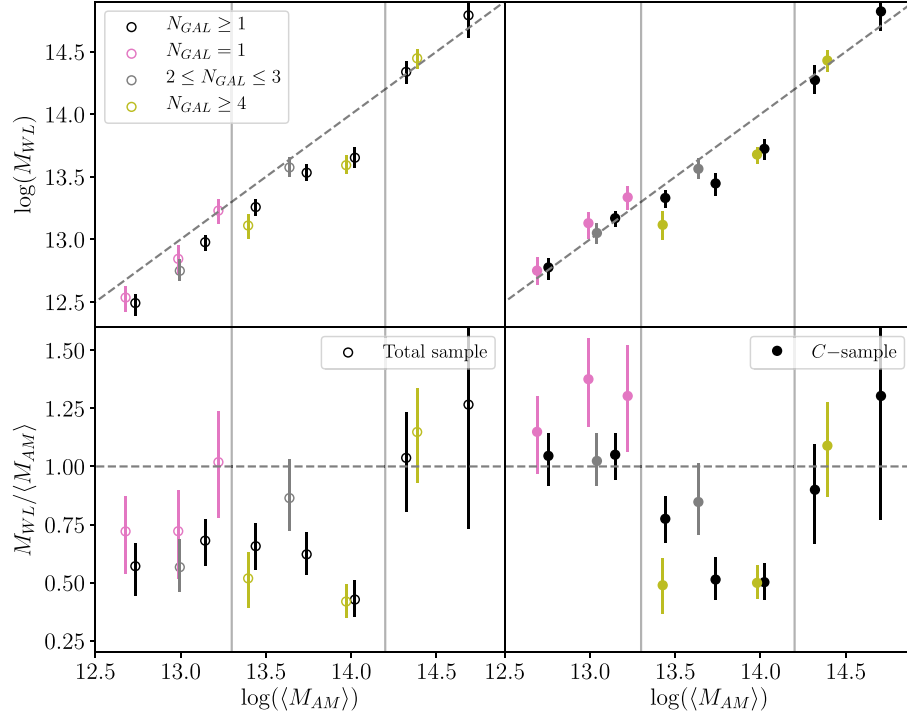


**Figure 5.**  $M_{WL}$  lensing estimate (upper panels) and ratio between both mass estimates (bottom panels) versus the average  $M_{AM}$ , for the different samples analysed detailed in Table 1. In the left-hand panel, we show the results for the total sample using open circles and in the right-hand panel for the C-sample with filled circles. Dashed grey line corresponds to the identity and vertical lines represent the limits for the low-, intermediate-, and high-mass ranges. Masses are expressed in units of  $\log(h^{-1} M_{\odot})$ .

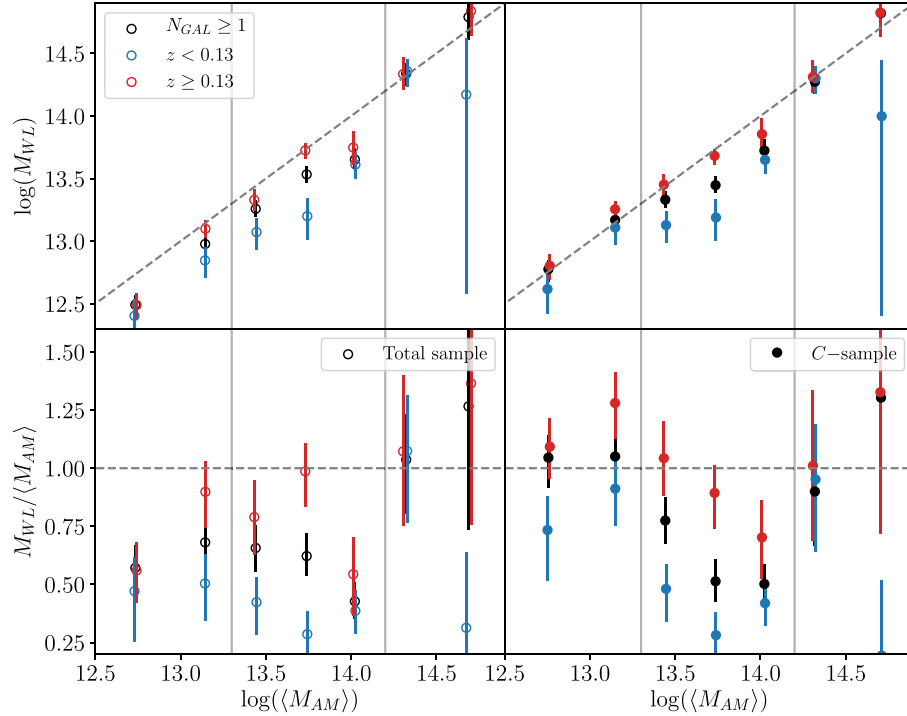


**Figure 6.**  $M_{WL}$  lensing estimate (upper panels) and ratio between both mass estimates (bottom panels) versus the average  $M_{AM}$ , for the subsamples selected according to the galaxy group redshift detailed in Table 2 and the subsamples without richness restriction ( $N_{GAL} \geq 1$ ) detailed in Table 1. In the left-hand panel, we show the results for the total sample using open circles and in the right-hand panel for the C-sample with filled circles. Dashed grey line corresponds to the identity and vertical lines represent the limits for the low-, intermediate-, and high-mass ranges. Masses are expressed in units of  $\log(h^{-1} M_{\odot})$ .

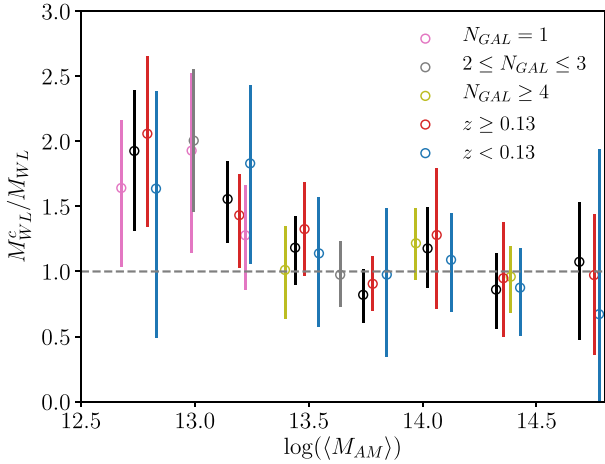


**Figure 7.** Mass ratio for the subsamples selected considering the whole sample of groups,  $M_{WL}$ , and the groups included in the  $C$ -sample ( $M_{WL}^c$ ), related to the average abundance matching mass. Values for the  $z \geq 0.13$  and  $z < 0.13$  subsamples (red and blue dots) are shifted in the  $x$ -axis by 0.05 and 0.10 for a better visualization.

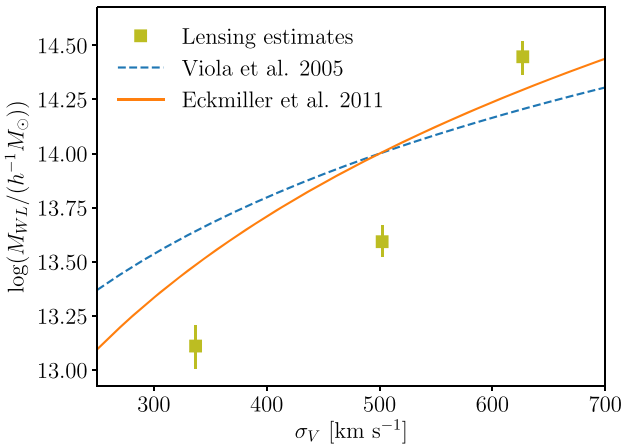


**Figure 8.** Comparison between the median LOS velocity dispersion,  $\sigma_v$ , and derived lensing mass estimates,  $M_{WL}$ , for groups with more than four members (yellow squares). Dashed blue line corresponds to the relation derived by Viola et al. (2015) between lensing mass estimates and the velocity dispersions for a sample of galaxy groups ( $M_{WL}/(10^{14} h^{-1} M_\odot) = (\sigma_v/(500 \text{ km s}^{-1}))^{1.89}$ ). The shaded blue region corresponds to the reported dispersion ( $\sigma_{\log(M_{WL})} = 0.2$ ). In solid orange line, we show the predicted relation according to numerical simulations ( $M_{200}/(10^{14} h^{-1} M_\odot) = (\sigma_v/(500 \text{ km s}^{-1}))^3$ , Eckmiller et al. 2011).

## 5 SUMMARY AND DISCUSSION

In this work, we have presented a weak-lensing mass analysis of a galaxy group sample in the redshift range  $0.05 < z < 0.2$ , identified using a combination of FOF and halo-based methods. The group sample considered spans over a wide mass range, with  $M_{WL}$  masses ranging from  $10^{12.5} h^{-1} M_\odot$  to  $10^{14.7} h^{-1} M_\odot$ . In order to explore the relation between the masses assigned according to the abundance matching technique,  $M_{AM}$ , and the lensing estimates, we split the total sample of groups in subsamples of  $\log(M_{AM})$  bins. We also considered different subsamples selected according to the group richness,  $N_{GAL}$ , and redshift.

For the lensing analysis, we applied stacking techniques and combined four public lensing catalogues in order to improve the signal-to-noise ratio. Lensing profiles were obtained by assuming that the BGM is located at the halo centre. We modelled the profiles by considering two free parameters, the fraction of well-centred groups,  $p_{cc}$ , and the NFW mass,  $M_{WL}$ .

According to a mock sample of groups identified in numerical simulations, the fractions of well-centred groups derived from the lensing analysis are in agreement with the ones expected due to uncertainties in the membership assignment. Nevertheless, lensing estimates of the fraction of centred groups are mainly biased to lower values, specially for the higher mass subsamples. This result may be due to the inclusion of a larger fraction of merging systems in these subsamples.

Lensing masses obtained for the different subsamples of groups considered correlate well with the average abundance matching estimates. This result provides observational evidence of a tight correlation between the halo mass and the characteristic group luminosity. Therefore, it supports the use of the group luminosity as a mass proxy, specially for low massive systems. However, masses based on the group luminosity tend to predict higher values than the determined by the weak-lensing analysis, for low- and intermediate-mass groups ( $\langle M_{AM} \rangle < 10^{14.2} h^{-1} M_\odot$ ). When considering only the groups with an early-type central galaxy selected according to the concentration index, the agreement between lensing masses and  $M_{AM}$  improves significantly in the low-mass regime ( $\langle M_{AM} \rangle < 10^{13.3} h^{-1} M_\odot$ ). This behaviour is observed for all the subsamples included in this mass range, regardless of the richness and redshift group. Since it is expected that early-type galaxies are associated with denser environments (Dressler 1980; Postman & Geller 1984; Balogh et al. 2004; Kauffmann et al. 2004), considering this proxy for the group selection could improve the identification. Also, a higher dispersion of the luminosity–halo mass relation is expected for this mass range (Yang et al. 2005). It is important to take into account that the abundance matching relies on an oversimplified one-to-one relation between the characteristic luminosity of each group and the halo mass, which neglects the effects of possible biases introduced by other properties such as the morphology or colours of the member galaxies.

For intermediate-mass groups ( $10^{13.3} h^{-1} M_\odot < \langle M_{AM} \rangle < 10^{14.2} h^{-1} M_\odot$ ), lensing masses are systematically biased to lower values for all the subsamples considered. For this mass range, we also find masses to be biased towards lower values for groups at lower redshifts ( $z < 0.13$ ). When splitting the subsamples according to group richness, the bias in this mass range prevails only for the groups with more than three members. Since at this richness and mass range we expect higher uncertainties in membership assignment, it can be argued that a significant inclusion of interlopers are affecting the characteristic luminosity assigned. This could also explain the observed bias in the low-redshift subsamples since at this mass and redshift range, 75 per cent of the groups have  $N_{GAL} \geq 4$ .

Finally, for the high-mass groups ( $\langle M_{AM} \rangle > 10^{14.2} h^{-1} M_\odot$ ), we obtain a good agreement between mass estimates for all the considered subsamples. This is in agreement with a more constrained relation between the group luminosity and the halo mass for the systems with higher masses (Kang et al. 2005), favouring the one-to-one relation in which the abundance matching mass is based.

In addition with a possible bias introduced by interlopers in the galaxy group identification, the observed discrepancies between predicted masses based on the group luminosity and the derived according to the lensing study, can be also related with the intrinsic scatter between the luminosity and the halo mass. A deep inspection

between possible bias introduced in the mass assignment according to the group characteristic luminosity using hydrodynamic simulations can help to assess the observed differences. On the other hand, the analysis of a larger group sample which will increase the lensing signal, thus allowing an improvement in the modelling of the profiles, can also provide better constrained lensing masses to discard possible bias introduced in the study.

We have also compared our lensing masses to the median LOS velocity dispersion of the subsamples of groups with more than four members. As for the abundance matching mass comparison, lensing masses for groups in the intermediate-mass range are biased to lower values, compared with the median velocity dispersion predicted by simulations. Once again, the inclusion of interlopers might be biasing the observed LOS velocity dispersion,  $\sigma_v$ , to higher values. We highlight that the derived good correlation between both parameters indicates that  $\sigma_v$  also provides a good proxy for the halo masses, but its limited to systems with more than four members.

The results derived by the analyses presented in this work can serve as important tests for the mass-proxy estimates in a wide mass range of galaxy systems. A well calibrated mass-proxy that can constrain the mean halo masses is important in order to better characterize galaxy systems and to use them as cosmological probes. Although there is still a long way ahead in order to quantify the possible biases introduced, this work supports the use of abundance matching techniques for mass estimates of diverse samples of galaxy systems.

## ACKNOWLEDGEMENTS

We are highly thankful to the anonymous referee for their useful comments, which helped to improve this paper. This work was partially supported by the Consejo Nacional de Investigaciones Científicas y Técnicas (CONICET, Argentina), the Secretaría de Ciencia y Tecnología de la Universidad Nacional de Córdoba (SeCyT-UNC, Argentina), the Brazilian Council for Scientific and Technological Development (CNPq), and the Rio de Janeiro Research Foundation (FAPERJ). We acknowledge the PCI BEV fellowship program from MCTI and CBPF. MM acknowledges FAPERJ and CNPq for financial support. FORA BOZO. This work is based on observations obtained with MegaPrime/MegaCam, a joint project of *CFHT* and CEA/DAPNIA, at the *Canada–France–Hawaii Telescope (CFHT)*, which is operated by the National Research Council (NRC) of Canada, the Institut National des Sciences de l'Univers of the Centre National de la Recherche Scientifique (CNRS) of France, and the University of Hawaii. The Brazilian partnership on *CFHT* is managed by the Laboratório Nacional de Astrofísica (LNA). We thank the support of the Laboratório Interinstitucional de e-Astronomia (LInEA). We thank the CFHTLenS team for their pipeline development and verification upon which much of the CS82 survey pipeline was built.

This research used the facilities of the Canadian Astronomy Data Centre operated by the National Research Council of Canada with the support of the Canadian Space Agency. RCSLenS data processing was made possible thanks to significant computing support from the NSERC Research Tools and Instruments grant program. Based on data products from observations made with *ESO* Telescopes at the La Silla Paranal Observatory under programme IDs 177.A-3016, 177.A-3017, and 177.A-3018.

## DATA AVAILABILITY

The data sets were derived from sources in the public domain: CFHTLenS (<http://www.cadc-ccda.hia-ihc.nrc-cnrc.gc.ca/en/community/CFHTLenS>), RCSLenS (<https://www.ca>

[dc-ccda.hia-ihc.nrc-cnrc.gc.ca/en/community/rcslens](http://dc-ccda.hia-ihc.nrc-cnrc.gc.ca/en/community/rcslens)), KiDS-450 (<http://kids.strw.leidenuniv.nl/cosmicshear2018.php>), and redMaP-Per (<http://risa.stanford.edu/redmapper/>). CS82 can be accessed on request by emailing to [martincbpf.br](mailto:martincbpf.br). The data derived in this article are available on request to the corresponding author.

## REFERENCES

- Alam S. et al., 2015, *ApJS*, 219, 12  
 Allen S. W., Evrard A. E., Mantz A. B., 2011, *ARA&A*, 49, 409  
 Alpaslan M. et al., 2012, *MNRAS*, 426, 2832  
 Annis J. et al., 2014, *ApJ*, 794, 120  
 Applegate D. E. et al., 2014, *MNRAS*, 439, 48  
 Balogh M. L., Baldry I. K., Nichol R., Miller C., Bower R., Glazebrook K., 2004, *ApJ*, 615, L101  
 Bartelmann M., 1995, *A&A*, 303, 643  
 Behroozi P. S., Conroy C., Wechsler R. H., 2010, *ApJ*, 717, 379  
 Bellagamba F., Roncarelli M., Maturi M., Moscardini L., 2018, *MNRAS*, 473, 5221  
 Benítez N., 2000, *ApJ*, 536, 571  
 Berlind A. A. et al., 2006, *ApJS*, 167, 1  
 Boulade O. et al., 2003, in Iye M., Moorwood A. F. M., eds, *MegaCam: the new Canada-France-Hawaii Telescope wide-field imaging camera*, Vol. 4841, Instrument Design and Performance for Optical/Infrared Ground-based Telescopes, SPIE, p. 72  
 Bundy K., Leauthaud A., Saito S., Maraston C., Wake D. A., Thomas D., 2017, *ApJ*, 851, 34  
 Chalela M., Gonzalez E. J., Makler M., García Lambas D., Pereira M. E. S., O'Mill A. L., Shan H., 2018, *MNRAS*, 479, 1170  
 Chalela M., Sillero E., Pereyra L., García M. A., Cabral J. B., Lares M., Merchán M., 2019, *Astronomy and Computing*, 34, 100443  
 Coe D., Benítez N., Sánchez S. F., Jee M., Bouwens R., Ford H., 2006, *AJ*, 132, 926  
 Conroy C., Wechsler R. H., Kravtsov A. V., 2006, *ApJ*, 647, 201  
 Cristofari P., Ostriker J. P., 2019, *MNRAS*, 482, 4364  
 Dressler A., 1980, *ApJ*, 236, 351  
 Duffy A. R., Schaye J., Kay S. T., Dalla Vecchia C., 2008, *MNRAS*, 390, L64  
 Durret F. et al., 2015, *A&A*, 578, A79  
 Ekmiller H. J., Hudson D. S., Reiprich T. H., 2011, *A&A*, 535, A105  
 Erben T. et al., 2013, *MNRAS*, 433, 2545  
 Evrard A. E. et al., 2008, *ApJ*, 672, 122  
 Fenech Conti I., Herbonnet R., Hoekstra H., Merten J., Miller L., Viola M., 2017, *MNRAS*, 467, 1627  
 Finoguenov A. et al., 2015, *A&A*, 576, A130  
 Ford J., Hildebrandt H., Van Waerbeke L., Erben T., Laigle C., Milkeraitis M., Morrison C. B., 2014, *MNRAS*, 439, 3755  
 Foreman-Mackey D., Hogg D. W., Lang D., Goodman J., 2013, *PASP*, 125, 306  
 Gal R. R., Lopes P. A. A., de Carvalho R. R., Kohl-Moreira J. L., Capelato H. V., Djorgovski S. G., 2009, *AJ*, 137, 2981  
 Gilbank D. G., Gladders M. D., Yee H. K. C., Hsieh B. C., 2011, *AJ*, 141, 94  
 Gladders M. D., Yee H. K. C., 2000, *AJ*, 120, 2148  
 Gonzalez E. J., Makler M., Garcia Lambas D., Chalela M., Pereira M. E. S., Van Waerbeke L., Shan H., Erben T., 2020, *MNRAS*, 501, 5239  
 Guo Q., White S., Li C., Boylan-Kolchin M., 2010, *MNRAS*, 404, 1111  
 Han J. et al., 2015, *MNRAS*, 446, 1356  
 Hand N. et al., 2015, *Phys. Rev. D*, 91, 062001  
 Heymans C. et al., 2012, *MNRAS*, 427, 146  
 Hildebrandt H. et al., 2012, *MNRAS*, 421, 2355  
 Hildebrandt H. et al., 2016, *MNRAS*, 463, 635  
 Hildebrandt H. et al., 2017, *MNRAS*, 465, 1454  
 Hoekstra H., 2007, *MNRAS*, 379, 317  
 Hoekstra H., Herbonnet R., Muzzin A., Babul A., Mahdavi A., Viola M., Cacciato M., 2015, *MNRAS*, 449, 685  
 Huchra J. P., Geller M. J., 1982, *ApJ*, 257, 423  
 Johnston D. E. et al., 2007, preprint ([arXiv:0709.1159](https://arxiv.org/abs/0709.1159))  
 Kang X., Jing Y. P., Mo H. J., Börner G., 2005, *ApJ*, 631, 21



Kauffmann G., White S. D. M., Heckman T. M., Ménard B., Brinchmann J., Charlot S., Tremonti C., Brinkmann J., 2004, *MNRAS*, 353, 713

Kettula K. et al., 2013, *ApJ*, 778, 74

Kitching T. D., Miller L., Heymans C. E., van Waerbeke L., Heavens A. F., 2008, *MNRAS*, 390, 149

Kneib J.-P. et al., 2003, *ApJ*, 598, 804

Kravtsov A. V., Borgani S., 2012, *ARA&A*, 50, 353

Kravtsov A. V., Berlind A. A., Wechsler R. H., Klypin A. A., Gottlöber S., Allgood B. O., Primack J. R., 2004, *ApJ*, 609, 35

Kuijken K. et al., 2015, *MNRAS*, 454, 3500

Lawrence A. et al., 2007, *MNRAS*, 379, 1599

Le Brun A. M. C., McCarthy I. G., Schaye J., Ponman T. J., 2014, *MNRAS*, 441, 1270

Leauthaud A. et al., 2010, *ApJ*, 709, 97

Leauthaud A. et al., 2017, *MNRAS*, 467, 3024

Licitra R., Mei S., Raichoor A., Erben T., Hildebrandt H., 2016, *MNRAS*, 455, 3020

Liu X. et al., 2015, *MNRAS*, 450, 2888

McClintock T. et al., 2019, *MNRAS*, 482, 1352

Melchior P. et al., 2017, *MNRAS*, 469, 4899

Merchán M., Zandivarez A., 2002, *MNRAS*, 335, 216

Merchán M. E., Zandivarez A., 2005, *ApJ*, 630, 759

Milkeraitis M., van Waerbeke L., Heymans C., Hildebrandt T. H., Dietrich J. P., Erben T., 2010, *MNRAS*, 406, 673

Miller L. et al., 2013, *MNRAS*, 429, 2858

Miller L., Kitching T. D., Heymans C., Heavens A. F., van Waerbeke L., 2007, *MNRAS*, 382, 315

Miller C. J. et al., 2005, *AJ*, 130, 968

Moore B., Frenk C. S., White S. D. M., 1993, *MNRAS*, 261, 827

Murphy D. N. A., Geach J. E., Bower R. G., 2012, *MNRAS*, 420, 1861

Navarro J. F., Frenk C. S., White S. D. M., 1997, *ApJ*, 490, 493

Oguri M., 2014, *MNRAS*, 444, 147

Pearson R. J., Ponman T. J., Norberg P., Robotham A. S. G., Farr W. M., 2015, *MNRAS*, 449, 3082

Pereira M. E. S. et al., 2018, *MNRAS*, 474, 1361

Pereira M. E. S. et al., 2020, *MNRAS*, 498, 5450

Postman M., Geller M. J., 1984, *ApJ*, 281, 95

Radovich M. et al., 2017, *A&A*, 598, A107

Rodriguez F., Merchán M., 2020, *A&A*, 636, A61

Rodriguez F., Merchán M., Sgró M. A., 2015, *A&A*, 580, A86

Rodriguez F., Gonzalez E. J., O'Mill A. L., Gaztañaga E., Fosalba P., Lambas D. G., Mezcuca M., Siudek M., 2020, *A&A*, 634, A123

Rykoff E. S. et al., 2014, *ApJ*, 785, 104

Schrabback T. et al., 2020, *AAP*, 646, A73

Shan H. Y. et al., 2014, *MNRAS*, 442, 2534

Sheldon E. S. et al., 2004, *AJ*, 127, 2544

Simet M., McClintock T., Mandelbaum R., Rozo E., Rykoff E., Sheldon E., Wechsler R. H., 2017, *MNRAS*, 466, 3103

Soares-Santos M. et al., 2011, *ApJ*, 727, 45

Springel V. et al., 2005, *Nature*, 435, 629

Stratava I. et al., 2001, *AJ*, 122, 1861

Sun M., Voit G. M., Donahue M., Jones C., Forman W., Vikhlinin A., 2009, *ApJ*, 693, 1142

Tasitsiomi A., Kravtsov A. V., Wechsler R. H., Primack J. R., 2004, *ApJ*, 614, 533

Tempel E., Tago E., Liivamägi L. J., 2012, *A&A*, 540, A106

Tucker D. L. et al., 2000, *ApJS*, 130, 237

Vale A., Ostriker J. P., 2004, *MNRAS*, 353, 189

van Breukelen C., Clewley L., 2009, *MNRAS*, 395, 1845

Varga T. N. et al., 2019, *MNRAS*, 489, 2511

Viola M. et al., 2015, *MNRAS*, 452, 3529

Warren M. S., Abazajian K., Holz D. E., Teodoro L., 2006, *ApJ*, 646, 881

Wen Z. L., Han J. L., Liu F. S., 2012, *ApJS*, 199, 34

Wright C. O., Brainerd T. G., 2000, *ApJ*, 534, 34

Xia Q. et al., 2020, *A&A*, 633, A89

Yan Z., Raza N., Van Waerbeke L., Mead A. J., McCarthy I. G., Tröster T., Hinshaw G., 2020, *MNRAS*, 493, 1120

Yang X., Mo H. J., van den Bosch F. C., Jing Y. P., 2005, *MNRAS*, 356, 1293

Yang X., Mo H. J., van den Bosch F. C., Jing Y. P., Weinmann S. M., Meneghetti M., 2006, *MNRAS*, 373, 1159

Yang X., Mo H. J., van den Bosch F. C., Pasquali A., Li C., Barden M., 2007, *ApJ*, 671, 153

## APPENDIX A: MASS ESTIMATES DERIVED FOR THE INDIVIDUAL LENSING SURVEYS

In order to test the combination of the shear catalogues used for the analysis and presented in Section 2, we derive the  $M_{WL}$  by fitting the profiles computed using the individual lensing catalogues combined in this work (CFHTLenS, CS82, RCSLenS, and KiDS-450). Profiles were obtained by selecting the groups from the total group sample ( $N_{GAL} \geq 1$ ) according to the  $\log M_{AM}$  bins specified in Table 1. In Table A1, we show the number of groups considered for the stacking in each bin and lensing survey. In Fig. A1, we plot the relation between the mean  $M_{AM}$  and lensing estimates using the individual surveys. According to this comparison, not significant biases are observed in the computed masses.

## APPENDIX B: 2D PROBABILITY DISTRIBUTIONS

We show in Figs B1 and B2 the posterior distribution of the fitted parameters  $\log(M_{WL})$  and  $p_{cc}$  for the total sample binned according

**Table A1.** Columns: (1)  $\log M_{AM}$  bins; (2), (3), (4), and (5) Number of groups in each bin considered for the stacking using the correspondent lensing catalog.

$\log M_{AM}$	CFHT	CS82	KiDS-450	RCSLenS
[12.5, 13.0]	1405	2848	5412	4481
[13.0, 13.3]	322	729	1295	1132
[13.3, 13.6]	148	337	581	490
[13.6, 13.9]	64	132	244	200
[13.9, 14.2]	24	50	105	85
[14.2, 14.5]	7	21	20	33
[14.5, 15.0]	2	0	4	3

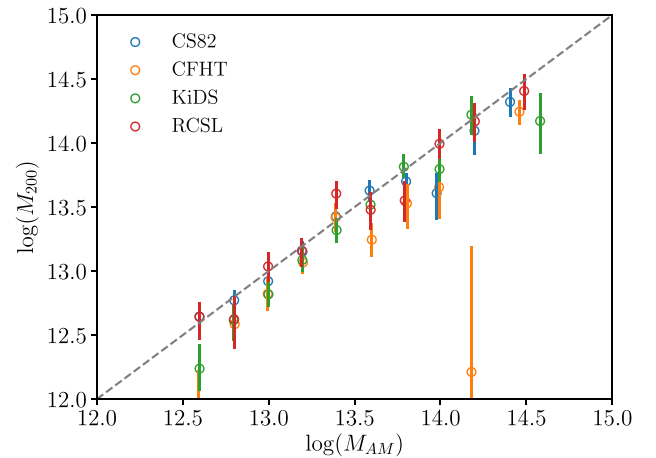


**Figure A1.** Fitted lensing masses derived using the individual shear data sets versus the average  $M_{AM}$ .

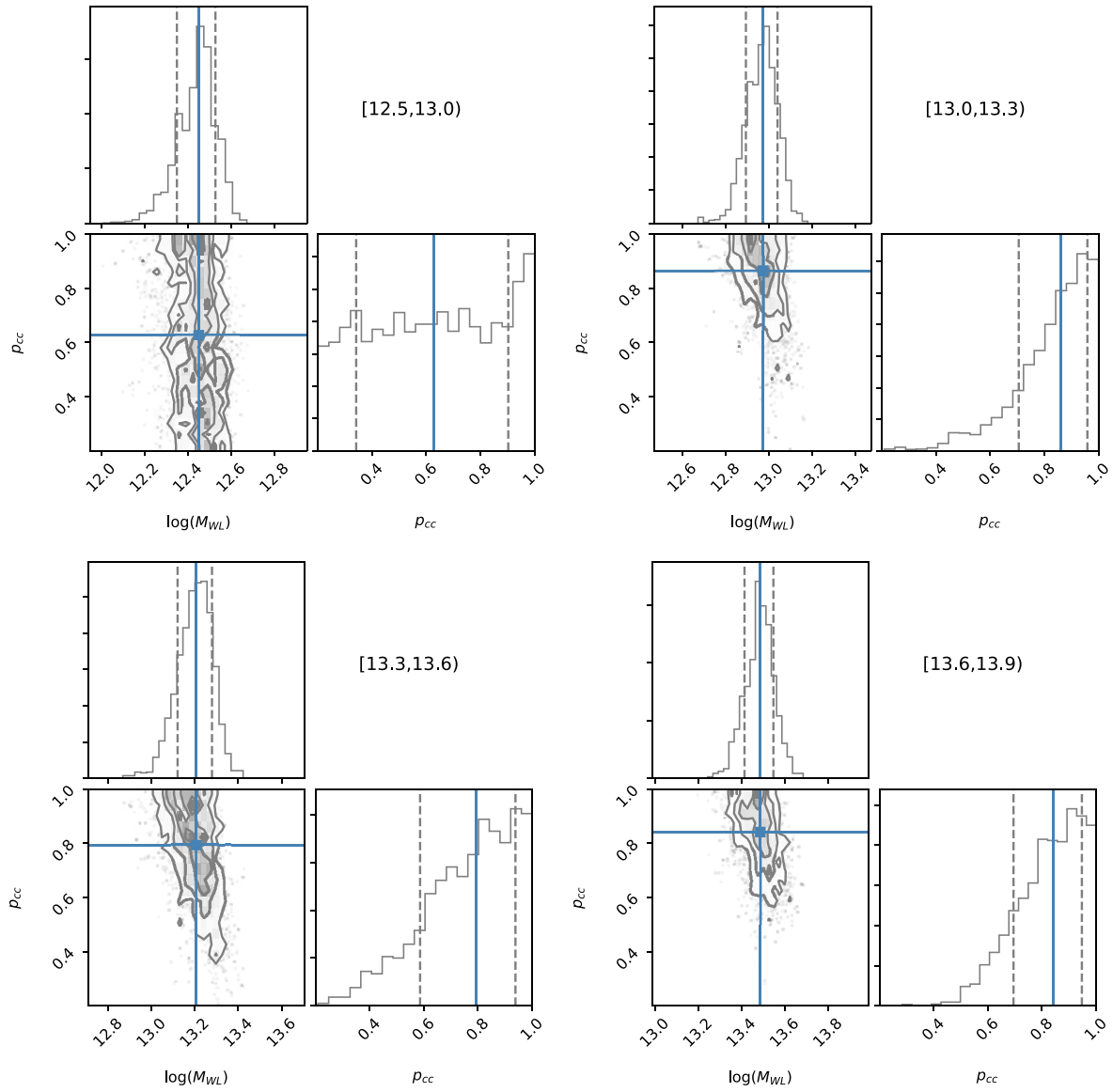


**Figure B1.** 1D and 2D projections of the posterior probability distributions of the fitted parameters,  $\log(M_{WL})$  and  $p_{cc}$ , for the first four bins described in Table 1. Solid line represents the adopted median value while dashed lines correspond to the 16th and 84th percentiles.

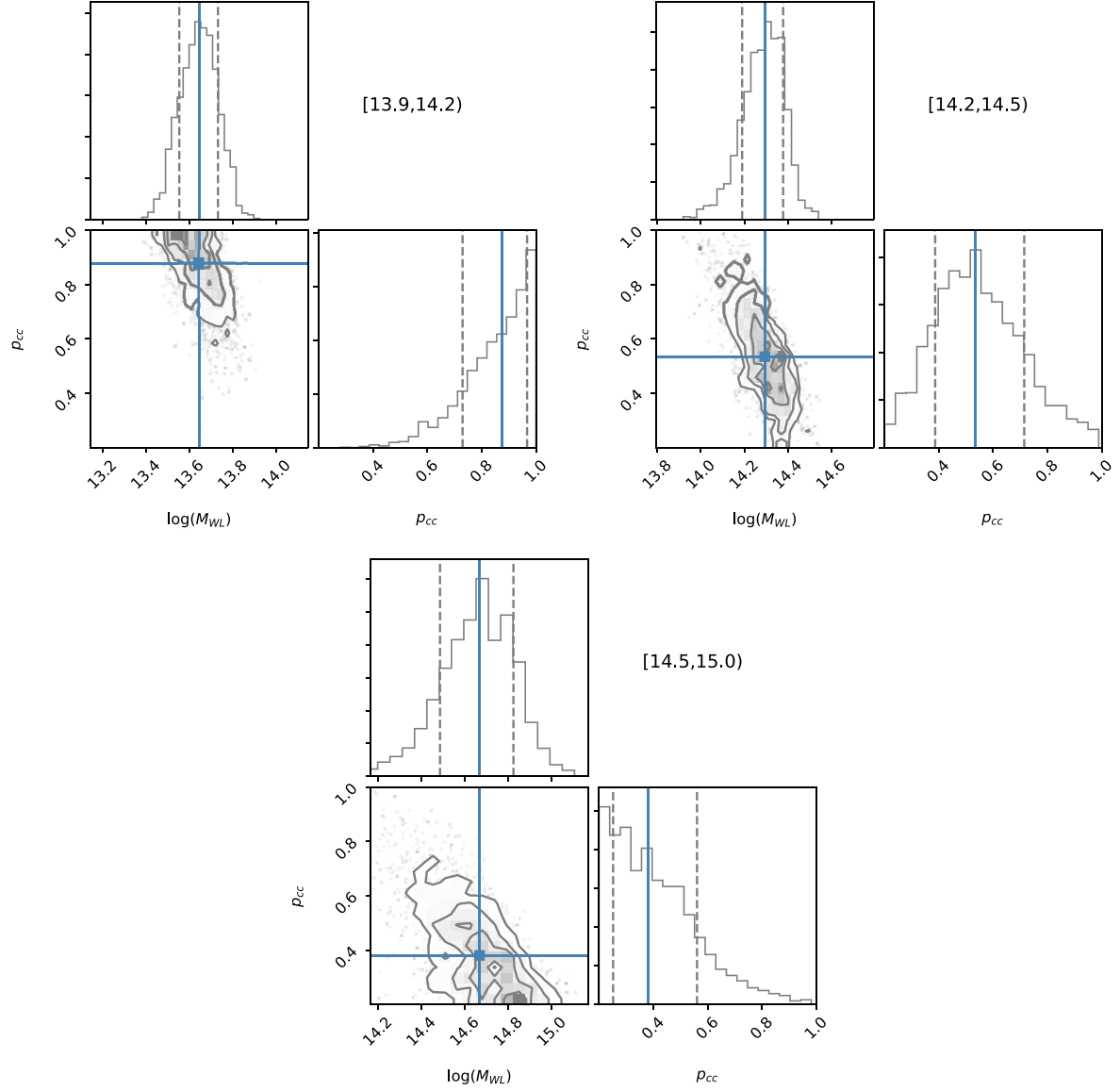


**Figure B2.** 1D and 2D projections of the posterior probability distributions of the fitted parameters,  $\log(M_{\text{WL}})$  and  $p_{\text{cc}}$ , for the latest three bins described in Table 1. Solid line represents the adopted median value while dashed lines correspond to the 16th and 84th percentiles.

the described bins in Table 1, with no restriction in richness ( $N_{\text{GAL}} \geq 1$ ).

### APPENDIX C: LUMINOSITY DISTRIBUTIONS

In this appendix, we detail the characteristic luminosity distributions,  $L_{\text{gr}}$ , for each subsample considered for the stacking in the lensing

analysis. We show the distributions in the Figs C1, C2, C3, and C4 for the total sample and C-sample selected according to the assigned abundance matching mass, richness, and redshift. In Tables C1 and C2, we give the median values and 16th and 84th percentiles of each selected subsample of groups.

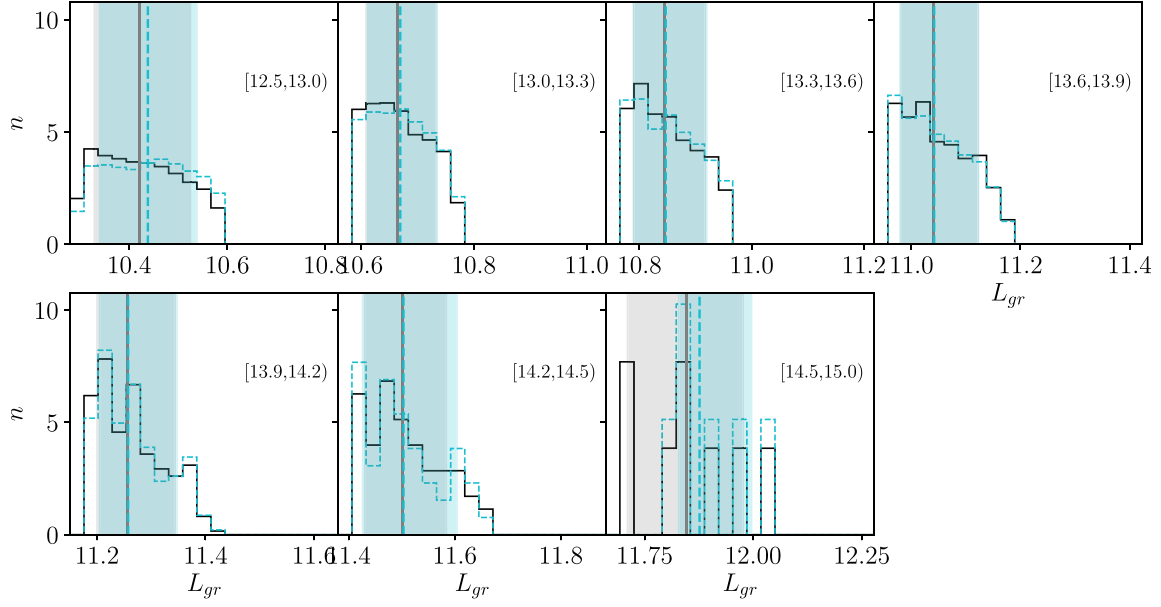


**Figure C1.** Normalized characteristic luminosity group distributions,  $L_{gr}$ , for the total (black solid line) and C-samples (cyan dashed line) selected in the  $\log M_{AM}$  ranges indicated in each panel. Vertical lines correspond to the median values and the shadow region enclose 15th and 85th percentiles. These samples correspond to the first seven rows described in Table C1, in the whole richness and redshift range ( $N_{GAL} \geq 1$  and  $0.05 \leq z < 0.2$ ).

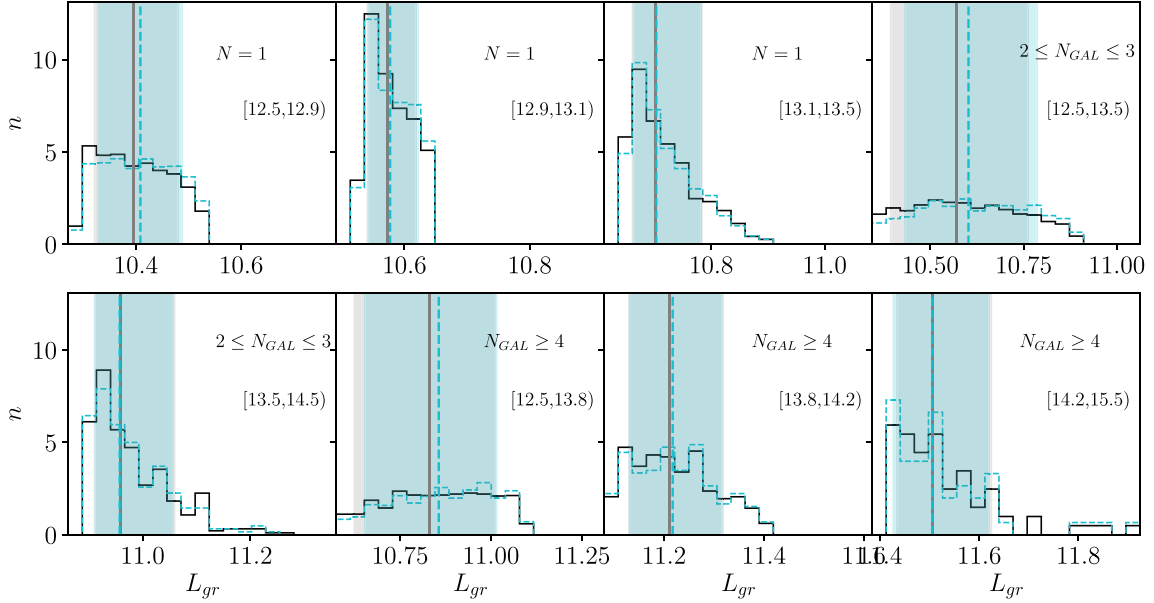


**Figure C2.** Normalized characteristic luminosity group distributions,  $L_{gr}$ , for the total (black solid line) and C-samples (cyan dashed line) selected in the  $\log M_{AM}$  ranges indicated in each panel. Vertical lines correspond to the median values and the shadow region enclose 15th and 85th percentiles. These samples correspond to the last eight rows described in Table C1, in the whole richness and redshift range ( $N_{GAL} \geq 1$  and  $0.05 \leq z < 0.2$ ) and in the richness range indicated in each panel.



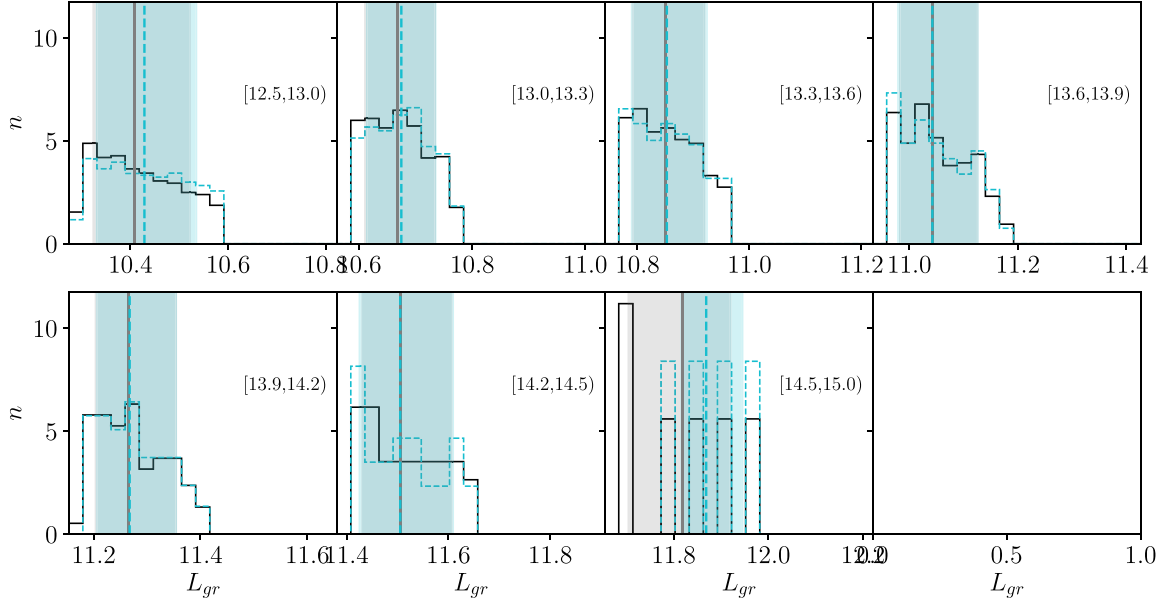


**Figure C3.** Normalized characteristic luminosity group distributions,  $L_{gr}$ , for the total (black solid line) and C-samples (cyan dashed line) selected in the  $\log M_{AM}$  ranges indicated in each panel. Vertical lines correspond to the median values and the shadow region enclose 15th and 85th percentiles. These samples correspond to the first seven rows described in Table C2, in the whole richness range and with  $0.05 \leq z < 0.13$ .

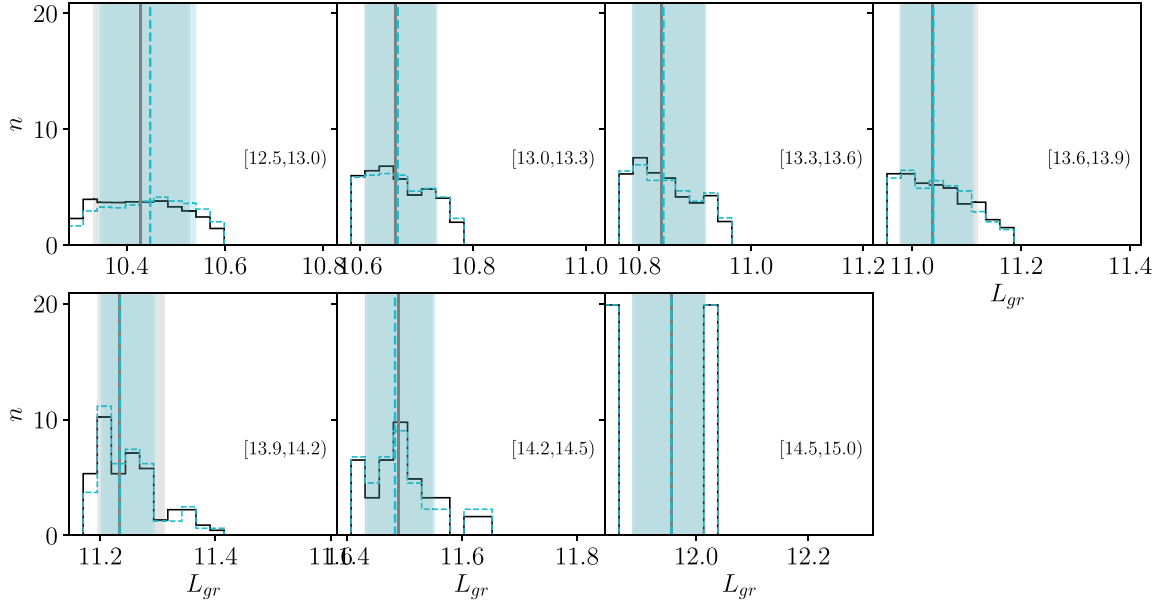


**Figure C4.** Normalized characteristic luminosity group distributions,  $L_{gr}$ , for the total (black solid line) and C-samples (cyan dashed line) selected in the  $\log M_{AM}$  ranges indicated in each panel. Vertical lines correspond to the median values and the shadow region enclose 15th and 85th percentiles. These samples correspond to the latest seven rows described in Table C2, in the whole richness range and with  $0.13 \leq z < 0.2$ .

**Table C1.** Fitted parameters for the analysed galaxy groups in the whole redshift range ( $0.05 \leq z < 0.2$ ).

Richness selection	$\log M_{\text{AM}}$	Total sample			C-sample		
		$L_{50}$	$L_{15}$	$L_{85}$	$L_{50}$	$L_{15}$	$L_{85}$
$N_{\text{GAL}} \geq 1$	[12.5, 13.0]	10.42	10.33	10.53	10.44	10.34	10.54
	[13.0, 13.3]	10.66	10.61	10.73	10.67	10.61	10.74
	[13.3, 13.6]	10.84	10.79	10.92	10.85	10.79	10.92
	[13.6, 13.9]	11.04	10.98	11.12	11.04	10.98	11.12
	[13.9, 14.2]	11.26	11.20	11.34	11.26	11.20	11.35
	[14.2, 14.5]	11.50	11.43	11.58	11.50	11.43	11.60
	[14.5, 15.0]	11.85	11.71	11.98	11.88	11.83	12.00
$N_{\text{GAL}} = 1$	[12.5, 12.9]	10.40	10.32	10.48	10.41	10.33	10.49
	[12.9, 13.1]	10.57	10.54	10.62	10.58	10.54	10.62
	[13.1, 13.5]	10.70	10.66	10.78	10.70	10.66	10.78
$2 \leq N_{\text{GAL}} \leq 3$	[12.5, 13.5]	10.57	10.39	10.76	10.60	10.43	10.79
	[13.5, 14.5]	10.96	10.91	11.06	10.96	10.91	11.06
$N_{\text{GAL}} \geq 4$	[12.5, 13.8]	10.83	10.62	11.01	10.86	10.65	11.02
	[13.8, 14.2]	11.21	11.13	11.32	11.22	11.13	11.32
	[14.2, 15.5]	11.51	11.43	11.62	11.51	11.43	11.62

Columns: (1) Richness range of the selected subsamples; (2) Selection criteria according to the abundance matching mass,  $M_{\text{AM}}$ ; (3), (4), and (5) median, 15th and 85th percentiles of the  $L_{\text{GR}}$  distribution in each bin, for the total sample of groups. (6), (7), and (8) same for the groups included in the C-sample.

**Table C2.** Fitted parameters for the analysed galaxy groups in the whole richness range ( $N_{\text{GAL}} \geq 1$ ).

Redshift selection	$\log M_{\text{AM}}$	Total sample			C-sample		
		$L_{50}$	$L_{15}$	$L_{85}$	$L_{50}$	$L_{15}$	$L_{85}$
$z < 0.13$	[12.5, 13.0]	10.41	10.32	10.52	10.43	10.33	10.54
	[13.0, 13.3]	10.67	10.61	10.73	10.67	10.61	10.74
	[13.3, 13.6]	10.85	10.79	10.92	10.85	10.79	10.92
	[13.6, 13.9]	11.04	10.98	11.13	11.04	10.98	11.13
	[13.9, 14.2]	11.26	11.20	11.36	11.27	11.21	11.35
	[14.2, 14.5]	11.51	11.43	11.61	11.51	11.43	11.61
	[14.5, 15.0]	11.82	11.70	11.92	11.87	11.82	11.95
$z \geq 0.13$	[12.5, 13.0]	10.43	10.33	10.53	10.45	10.35	10.54
	[13.0, 13.3]	10.66	10.61	10.73	10.67	10.61	10.74
	[13.3, 13.6]	10.84	10.79	10.92	10.84	10.79	10.92
	[13.6, 13.9]	11.04	10.98	11.12	11.04	10.98	11.11
	[13.9, 14.2]	11.23	11.20	11.31	11.23	11.20	11.29
	[14.2, 14.5]	11.49	11.43	11.55	11.48	11.43	11.55
	[14.5, 15.0]	11.96	11.89	12.02	11.96	11.89	12.02

Note. Columns: (1) Redshift range of the selected subsamples; (2) Selection criteria according to the abundance matching mass,  $M_{\text{AM}}$ ; (3), (4), and (5) median, 15th and 85th percentiles of the  $L_{\text{GR}}$  distribution in each bin, for the total sample of groups. (6), (7), and (8) same for the groups included in the C-sample.

This paper has been typeset from a  $\text{\LaTeX}$  file prepared by the author.